

1 The Thermo-Chemical and Physical Structure
2 beneath the North American Continent from
3 Bayesian Inversion of Surface-wave Phase Velocities

A. Khan¹, A. Zunino², F. Deschamps³

A. Khan, Institute of Geochemistry and Petrology, Swiss Federal Institute of Technology, Clausiusstrasse 25, 8092 Zürich, Switzerland (amir.khan@erdw.ethz.ch).

A. Zunino, Dipartimento per lo Studio del Territorio e delle sue Risorse, Sez. Geofisica, University of Genova, Viale Benedetto XV 5, 16132 Genova, Italy (andrea.zunino@dipteris.unige.it).

F. Deschamps, Institute of Geophysics, Swiss Federal Institute of Technology, Sonneggstr. 5, 8092 Zurich, Switzerland (frederic.deschamps@erdw.ethz.ch).

¹Institute of Geochemistry and Petrology,
Swiss Federal Institute of Technology,
Zurich, Switzerland.

²DipTeRis, University of Genova, Genova,
Italy.

³Institute of Geophysics, Swiss Federal
Institute of Technology, Zurich, Switzerland.

4 **Abstract.** We jointly invert local fundamental-mode and higher-order
5 surface-wave phase-velocities for radial models of the thermo-chemical and
6 anisotropic physical structure of the Earth's mantle to ~ 1000 km depth be-
7 neath the North American continent. Inversion for thermo-chemical state re-
8 lies on a self-consistent thermodynamic method whereby phase equilibria and
9 physical properties (P -, S -wave velocity and density) are computed as func-
10 tions of composition (in the Na_2O - CaO - FeO - MgO - Al_2O_3 - SiO_2 model system),
11 pressure and temperature. We employ a sampling-based strategy to solve the
12 non-linear inverse problem relying on a Markov chain Monte Carlo method
13 to sample the posterior distribution in the model space. A range of models
14 fitting the observations within uncertainties are obtained from which any statis-
15 tics can be estimated. To further refine sampled models we compute geoid
16 anomalies for a collection of these and compare with observations, exempli-
17 fying *a posteriori* filtering through the use of additional data. Our thermo-
18 chemical maps reveal the tectonically stable older eastern parts of North Amer-
19 ica to be chemically depleted (high Mg#) and colder ($>200^\circ\text{C}$) relative to
20 the active younger regions (western margin and oceans). In the transition
21 zone the thermo-chemical structure decouples from that of the upper man-
22 tle, with a thermal anomaly appearing beneath the cratonic area that likely
23 extends into the lower mantle. In the lower mantle no consistent large-scale
24 thermo-chemical heterogeneities are observed, although our results do sug-
25 gest distinct upper and lower mantle compositions. Concerning anisotropy

²⁶ structure, we find evidence for a number of distinct anisotropic layers per-
²⁷ vading the mantle, including transition zone and upper-most lower mantle.

1. Introduction

28 Seismic tomography has proven a powerful tool in its ability to provide information on
29 the internal structure of the Earth and has done much to advance our understanding of
30 its dynamics. Since its advent in the late 1970s [e.g. *Aki et al.*, 1977; *Sengupta & Toksöz*,
31 1977; *Dziewonski et al.*, 1977], images obtained from the latter have proceeded to reveal
32 features at an unprecedented level of resolution, laterally as radially, that is continuously
33 being improved [e.g. *Ritsema et al.*, 2010].

34 While there is good reason to believe that the large-scale global velocity structure is
35 relatively well-resolved, given current consensus among studies that employ different data
36 and modelling techniques [e.g. *Grand et al.*, 1997; *Masters et al.*, 2000; *Trampert &*
37 *Woodhouse*, 2001; *Boschi & Ekström*, 2002; *Shapiro & Ritzwoller*, 2002; *Romanowicz*,
38 2003; *Ritsema et al.*, 2004; *Panning & Romanowicz*, 2006; *Kustowski et al.*, 2008; *Rawlin-*
39 *son et al.*, 2010], there is less agreement with regard to the smaller scales [e.g. *Trampert &*
40 *Van der Hilst*, 2005]. This ambiguity results partly from the use of iterative least-squares
41 approaches that are based upon a linearized forward model to invert global or regional
42 seismic data. This potentially biases the resulting images of the Earth in the direction
43 of the particular starting model and regularization scheme chosen, whereby assessment of
44 reliable model parameter uncertainty estimates become complicated, in addition to com-
45 plicating direct comparison between models obtained from different studies [e.g. *Trampert*,
46 1998; *Boschi & Dziewonski*, 1999; *Shapiro & Ritzwoller*, 2002; *Trampert & Van der Hilst*,
47 2005; *Khan et al.*, 2010].

48 In recognition of this, a number of recent studies [e.g. *Shapiro & Ritzwoller*, 2002;

49 *Visser et al.*, 2008a,b; *Bodin et al.*, 2009; *Khan et al.*, 2009, 2010; *Mosca*, 2010] have
50 employed non-linear stochastic-based inversion methods. Stochastic approaches, which
51 typically rely on Markov chain Monte Carlo (MCMC) methods, have proven, in spite of
52 their computationally intensive nature, increasingly popular within the geophysical com-
53 munity, not only because of their versatility, but most importantly because of their ability
54 to provide quantitative measures of model resolution, uncertainty and non-uniqueness [e.g.
55 *Mosegaard & Sambridge*, 2002; *Sambridge & Mosegaard*, 2002 and references therein].

56 However, rather than invert for seismic wave speeds we propose to invert directly for
57 the fundamental parameters of interest, namely mantle composition and thermal state.
58 Indeed, with the present level of completion of the mineral physics database, enabling
59 quantitative inferences to be made, a series of past studies using a variety of techniques
60 have focused on the problem of constraining mantle chemistry and thermal state using
61 geophysical data [e.g. *Deschamps & Trampert*, 2003; *Perry et al.*, 2003; *Trampert et al.*,
62 2004; *Shapiro & Ritzwoller*, 2004; *Kuskov et al.*, 2006, 2011; *Cammarano et al.*, 2009;
63 *Khan et al.*, 2009, 2010; *Cobden et al.*, 2008; *Ritsema et al.*, 2009]. Our approach, which
64 has been detailed previously [e.g. *Khan et al.*, 2007], makes use of a self-consistent ther-
65 modynamic methodology [*Connolly*, 2005] to systematically compute phase equilibria,
66 seismic wave speeds and density that depend only on composition, pressure and temper-
67 ature.

68 It is the purpose of the present study to employ the Metropolis algorithm (a type of
69 MCMC method) to estimate thermo-chemical, physical and anisotropic structure beneath
70 the North American continent and adjacent easternmost part of the Pacific Ocean using
71 the global surface-wave phase-velocity maps of *Visser et al.* [2008a], which consist of

72 Rayleigh and Love-wave phase velocities of fundamental modes and overtones including
73 uncertainties (see next section for further discussion). The use of phase velocity maps
74 in place of the original phase velocity measurements, from which the former are derived,
75 should be considered a simplifying assumption for the purpose of rendering the current
76 study tractable. We pick the North American continent as it has been studied exten-
77 sively seismically [e.g. *Grand, 1994; Van der Lee & Nolet, 1997b; Goes & Van der Lee,*
78 *2002; Godey et al., 2004; Van der Lee & Frederiksen, 2005; Marone et al., 2007; Nettles*
79 *& Dziewonski, 2008; Sigloch et al., 2008; Tian et al., 2009; Yuan & Romanowicz, 2010;*
80 *Yuan et al., 2011*], providing a number of models with which to compare.

81 The immediate benefit of a wedlock between stochastic inversion and thermodynamic
82 modelling as envisioned here, include: 1) inversion of seismic data directly for thermo-
83 chemical structure, 2) quantitative assessment of model parameter uncertainties, resolu-
84 tion and non-uniqueness, 3) no potential bias through particular choice of initial/reference
85 model nor damping parameter/regularization scheme and 4) depending on the specific set
86 of seismic data considered, which typically are either sensitive to P or S -wave speed, we
87 simultaneously constrain P -, S -wave speed and density. In particular point 1) above is all-
88 important for unraveling the underlying nature of the processes that produce the observed
89 variations in seismic wave speeds seen in tomography images, inasmuch as it enables us
90 to distinguish between the relative contributions of composition and temperature, which
91 as yet are not fully understood.

92 A prominent asset of seismic tomography studies is a global or regional image of seismic
93 wave velocity. However, as it is not feasible to display images of all models sampled here,
94 we revert to the idea initiated by *Koren et al. [1991]* and further exemplified by *Mosegaard*

95 *É Tarantola* [1995] and *Tarantola* [2005] of employing the movie strategy, which entails
 96 extracting and displaying random samples from the prior and posterior probability dis-
 97 tributions. It is the contention here that the standard practice of looking at a single
 98 tomographic image should be abandoned in favour of an approach where several images
 99 are analyzed or interpreted concomitantly for current geoscientific implications of inter-
 100 est. This is a consequence of the fact that all models to be shown here are models with
 101 a high likelihood that fit data within uncertainties, but are likely to differ in terms of
 102 geodynamical implications. As a specific illustration of this we will compare observed
 103 geoid anomalies with those computed from the density (anomaly) maps obtained here.

104 Finally, we would like to dedicate this paper to the founding father of the probabilistic in-
 105 ference approach to inverse problems, the late Albert Tarantola, whose ideas on sampling-
 106 based methods for searching high-dimensional model parameter spaces and probabilistic
 107 treatment of inverse problems in general are at the heart of the present study (for an
 108 excellent summary account of Albert Tarantola's work we refer the reader to *Mosegaard*
 109 [2011]).

2. Surface-wave Dispersion Data

110 As data we consider the isotropic part (azimuthally averaged) of the global azimuthal
 111 anisotropic phase-velocity maps of fundamental and higher-mode Love (to 5th order) and
 112 Rayleigh (to 6th order) waves of *Visser et al.* [2008a], with a lateral resolution of $5^\circ \times 5^\circ$.
 113 The maps were obtained through an initial linear inversion of the global phase-delay
 114 database of *Visser et al.* We follow the approach of *Shapiro & Ritzwoller* [2004] and
 115 *Visser et al.* [2008b] and extract from the global surface-wave phase-velocity maps, on a
 116 $5^\circ \times 5^\circ$ -grid, dispersion curves (at the center of each pixel) for an area covering the North

117 American continent and surrounding, mostly Pacific, ocean (see figure 1). For each pixel
118 we thus have 13 dispersion curves consisting of a total of 149 distinct Love and Rayleigh-
119 wave phase-velocities as a function of frequency that we invert jointly for radial profiles
120 of composition, temperature and anisotropic structure underneath each $5^\circ \times 5^\circ$ pixel. We
121 limit ourselves to regional scale because of the high computational load inherent in the use
122 of MCMC methods, which at present prohibit a global-scale study at the above resolution.

123 We are aware of the limitations imposed on this study through our choice of surface-wave
124 phase-velocity maps rather than the original phase-velocity measurements ("tomographic
125 data") from which the former are constructed. The range of models that will be mapped
126 out here will to a large extent be controlled by the phase-velocity maps (data) and their
127 uncertainties, which, *a priori* are not necessarily representative of the uncertainties in-
128 herent in inversion of the "tomographic data". However, we would like to note that the
129 phase-velocity maps of *Visser et al.* [2008a] were constructed from phase-velocity mea-
130 surements obtained using a model space search technique, which, as deemed by *Visser et*
131 *al.* [2008a], provides consistent uncertainties on phase-velocity measurements as well as on
132 phase-velocity maps. Thus, although the present inversion is not a tomographic inversion
133 in *sensu stricto*, it is an inversion for a set of (local) radial profiles of thermo-chemical and
134 physical structure, which, when pieced together, result in a range of tomographic images
135 that are consistent with data, i.e. *Visser et al.*'s phase-velocity maps and uncertainties.

136 Although the inversion of maps in itself is undesirable, adherence to Monte Carlo meth-
137 ods for inverting data strongly limit the amount of unknowns one can invert for. Indeed,
138 with present computational resources available sampling-based strategies only allow for
139 low-resolution global seismic tomography models [e.g. *Mosca*, 2010; *Khan et al.*, 2010]

140 or models of limited geographical extent [e.g. *Bodin et al.*, 2009] and/or other modelling
 141 simplifications [e.g. *Shapiro et al.*, 2002]. However, the present approach should nonethe-
 142 less be considered a step toward future full resolution of the seismic tomography problem
 143 using non-linear strategies.

144 With regard to sensitivity of these waves they sense well into the upper part of the lower
 145 mantle (from hereon simply lower mantle) to a depth of ~ 1300 km. Moreover, while
 146 fundamental-mode surface-waves are predominantly sensitive to horizontally and verti-
 147 cally polarized S -wave velocity, the relative sensitivity of higher modes to compressional
 148 velocity (for Rayleigh-waves) and density grows with increasing overtone number [see
 149 *Anderson & Dziewonski*, 1982]. This difference in sensitivity of individual surface-wave
 150 modes allows us to simultaneously determine both thermal and compositional structure.
 151 Examples of dispersion curves will be shown later (see section 4.2, figure 2).

152

3. Parameterization and Forward Problem

153 Lateral variations in properties are defined over the grid shown in figure 1, with values
 154 defined at the center of each pixel, while radial variation is described using a number of
 155 layers, whose number varies depending on the particular property (this will be discussed
 156 further in section 4.1). Vertical layers beneath each pixel are described using the following
 157 set of parameters: 1) composition c , 2) temperature T , 3) anisotropy parameters ξ , ϕ and
 158 η (to be defined below), 4) seismic wave attenuation Q and 5) layer thicknesses. All the
 159 parameters are implicitly assumed to be functions of radius.

160 In order to compute isotropic physical properties (V_s, V_p, ρ) beneath each pixel of our
 161 lateral grid, given the fundamental parameters c and T , we employ a self-consistent ther-

162 modynamic method based on Gibbs free energy minimisation. We assume mantle mineral-
 163 ogy to be dictated by thermodynamic equilibrium and predict mineralogy as a function of
 164 composition, pressure, and temperature by Gibbs energy minimization using the method
 165 of Connolly (2005). For this purpose we adopt the thermodynamic formalism of Stixrude
 166 & Lithgow-Bertelloni (2005) as parameterized by Xu et al. (2008) for mantle minerals
 167 in the model chemical system $\text{Na}_2\text{O-CaO-FeO-MgO-Al}_2\text{O}_3\text{-SiO}_2$ (abbreviated NCFMAS).
 168 The Gibbs energy minimization procedure yields the amounts, compositions, and physical
 169 properties, including elastic moduli, of the stable minerals in the model chemical system.
 170 Aggregate elastic moduli are estimated from this information by Voigt-Reuss-Hill averag-
 171 ing.

172 Although we cannot really constrain attenuation structure Q with the surface-wave data
 173 here, we follow our previous approach [*Khan et al.*, 2010] and use the following expres-
 174 sion to estimate Q and thus anelastic contributions to the isotropic (anharmonic) P and
 175 S -wave velocities obtained using Gibbs free energy minimisation [e.g. *Anderson*, 1989;
 176 *Jackson*, 2000]

$$Q_\mu = Q_0 \exp \left[\frac{\alpha(E_a + pV_a)}{RT} \right] \quad (1)$$

177 where Q_0 is a constant, E_a activation energy, V_a activation volume, p pressure, T temper-
 178 ature, R the gas constant and α an exponent, which has been determined experimentally
 179 to be between 0.15-0.25 [*Jackson et al.*, 2002].

180 In relation to anisotropy, we follow the standard assumption adopted in most surface-
 181 wave tomography studies [e.g. *Panning & Romanowicz*, 2006; *Kustowski et al.*, 2008;
 182 *Nettles & Dziewonski*, 2008] and assume transverse anisotropy (symmetry axis in verti-
 183 cal direction). In order to compute Love and Rayleigh-wave dispersion curves, we first

184 need to compute $V_{sv}, V_{sh}, V_{pv}, V_{ph}$, which are velocities of vertically (v) and horizontally
 185 (h) polarized S -waves and vertically and horizontally propagating P -waves, respectively.
 186 Following the approach of previous surface-wave studies [e.g. *Panning & Romanowicz*,
 187 2006] and assuming that anisotropy is small ($\eta \sim 1$), anisotropic Voigt-averaged velocities
 188 can be computed from isotropic P and S -wave velocities [*Babuska & Cara*, 1991] using

$$V_{sv} = \sqrt{\frac{3V_s^2}{2\xi}}, \quad V_{sh} = \sqrt{\frac{3V_s^2}{2}}, \quad V_{ph} = \sqrt{\frac{5V_p^2}{4\phi}}, \quad V_{pv} = \sqrt{\frac{5V_p^2}{4}} \quad (2)$$

189 where ξ and ϕ quantify S and P -wave anisotropy, respectively, and η describes the depen-
 190 dence of velocity on the incidence angle of a propagating wave (Dziewonski & Anderson,
 191 1981). In summary, given values of the set of parameters $\{V_p, V_s, \xi, \phi, \eta\}$, anisotropic ve-
 192 locities are easily computed from expressions (2 & 3). Finally, we would like to recall that
 193 because we are considering surface-wave overtone data, sensitivity encompasses P -wave
 194 velocity and density in addition to S -wave velocity. Note also the complete absence of
 195 preassigned scaling factors between the various parameters.

4. Inverse Problem

196 As in our previous work we employ the probabilistic approach of *Tarantola & Valette*
 197 [1982] to solve the non-linear inverse problem. Within the Bayesian framework, the solu-
 198 tion to the general inverse problem $\mathbf{d} = \mathbf{g}(\mathbf{m})$ (\mathbf{d} is data vector and \mathbf{g} a typically non-linear
 199 operator that maps a model parameter vector \mathbf{m} into data), is given by [e.g. *Tarantola &*
 200 *Valette*, 1982; *Mosegaard & Tarantola*, 1995]

$$\sigma(\mathbf{m}) = kf(\mathbf{m})\mathcal{L}(\mathbf{m}), \quad (3)$$

201 where k is a normalization constant, $f(\mathbf{m})$ is the prior probability distribution on model
 202 parameters, i.e. information about model parameters obtained independently of data,

203 $\mathcal{L}(\mathbf{m})$ is the likelihood function, which in probabilistic terms can be interpreted as a
 204 measure of misfit between the observations and the predictions from model \mathbf{m} , and $\sigma(\mathbf{m})$ is
 205 the posterior model parameter distribution containing the solution to the inverse problem.
 206 The particular form of $\mathcal{L}(\mathbf{m})$ is determined by the observations, their uncertainties and
 207 how these are employed to model data noise.

208 In the current interdisciplinary context (see e.g. *Bosch* [1999] and *Khan et al.* [2007]
 209 for details) we are dealing with several different model parameters describing the system
 210 at various levels (physical - V_p & V_s , mineralogical/petrological - M (equilibrium modal
 211 mineralogy) and thermo-chemical - c & T). For present purposes we define three sets of
 212 parameters termed primary, secondary and tertiary model parameters (with the present
 213 general formulation this is easily generalised to any number of parameter vectors), which
 214 are given by $\mathbf{m}_p = \{c, T, \xi, \phi, \eta, Q\}$, $\mathbf{m}_s = \{M, V_p, V_s, \rho\}$ and $\mathbf{m}_t = \{V_{pv}, V_{ph}, V_{sv}, V_{sh}\}$,
 215 respectively. In the joint model parameter space $\mathcal{M} = \mathcal{M}_p \times \mathcal{M}_s \times \mathcal{M}_t$ we can define the
 216 joint model parameter vector $\mathbf{m} = \{\mathbf{m}_p, \mathbf{m}_s, \mathbf{m}_t\}$, where \mathcal{M}_p , \mathcal{M}_s and \mathcal{M}_t are primary,
 217 secondary and tertiary model parameter spaces, respectively. Extending eq. (3) to the
 218 joint description, we obtain

$$\sigma(\mathbf{m}_p, \mathbf{m}_s, \mathbf{m}_t) = kf(\mathbf{m}_p, \mathbf{m}_s, \mathbf{m}_t)\mathcal{L}(\mathbf{m}_p, \mathbf{m}_s, \mathbf{m}_t) \quad (4)$$

219 Note that since secondary parameters are functions of the primary model parameters and
 220 tertiary parameters are functions of both primary and secondary model parameters, the
 221 joint prior probability distribution and likelihood function can be suitably decomposed
 222 and dealt with separately by the rule of conditional probabilities. This is probably also
 223 warranted from the point of view that for most real problems the complexity of the joint
 224 prior density function is such that it generally would be difficult to formulate. Decom-

225 posing the joint prior then, we have

$$f(\mathbf{m}_p, \mathbf{m}_s, \mathbf{m}_t) = f_t(\mathbf{m}_t | \mathbf{m}_s, \mathbf{m}_p) f_s(\mathbf{m}_s | \mathbf{m}_p) f_p(\mathbf{m}_p) \quad (5)$$

226 where $f_p(\mathbf{m}_p)$ is a marginal probability density function (*pdf*) describing prior information
 227 on primary parameters, $f_s(\mathbf{m}_s | \mathbf{m}_p)$ and $f_t(\mathbf{m}_t | \mathbf{m}_s, \mathbf{m}_p)$ are conditional *pdfs* containing
 228 information about secondary and tertiary parameters and their dependence on primary
 229 and secondary parameters, respectively.

230 Let us assume that we have performed a number (k) of different geophysical experiments
 231 to study the system, structure or region of interest, with each of these giving rise to a set
 232 of observations $\mathbf{d}_1, \dots, \mathbf{d}_k$ belonging to the joint data parameter space $\mathcal{D} = \mathcal{D}_1 \times \dots \times \mathcal{D}_k$.
 233 Since, in general, observational uncertainties among different geophysical methods are
 234 independent we can write the joint likelihood function over the joint model space as

$$\mathcal{L}(\mathbf{m}_p, \mathbf{m}_s, \mathbf{m}_t) = \prod_{j=1,k} \mathcal{L}_j(\mathbf{m}_p, \mathbf{m}_s, \mathbf{m}_t) \quad (6)$$

235 where the \mathcal{L}_j are independent likelihood functions appropriate for each of the geophysical
 236 methods employed.

237 We can now summarize the posterior *pdf* in the joint model space by combining eqs. 4,
 238 5 and 6

$$\sigma(\mathbf{m}_p, \mathbf{m}_s, \mathbf{m}_t) = c f_t(\mathbf{m}_t | \mathbf{m}_s, \mathbf{m}_p) f_s(\mathbf{m}_s | \mathbf{m}_p) f_p(\mathbf{m}_p) \times \prod_{j=1,k} \mathcal{L}_j(\mathbf{m}_p, \mathbf{m}_s, \mathbf{m}_t) \quad (7)$$

239 To sample the posterior distribution (eq. (7)) in the joint model space we employ a
 240 Metropolis algorithm (a Markov chain Monte Carlo method). Although this algorithm is
 241 based on a random sampling of the model space, only models that result in a good data
 242 fit and are consistent with prior information are frequently sampled.

243 We employ the Metropolis-Hastings algorithm [*Metropolis et al.*, 1953; *Hastings*, 1970],
 244 which can be summarized in the following rules, to sample the joint posterior distribution
 245 (eq. 7) [e.g. *Mosegaard & Tarantola*, 1995]

246 1. Consider $\mathbf{m} = \{\mathbf{m}_p, \mathbf{m}_s, \mathbf{m}_t\}$ to be some current joint model in the Markov chain
 247 and randomly modify it to some candidate joint model $\mathbf{m}' = \{\mathbf{m}'_p, \mathbf{m}'_s, \mathbf{m}'_t\}$, where the
 248 candidate model is drawn from the prior using a proposal distribution.

249 2. Acceptance of \mathbf{m}' is governed by the probability

$$\mathcal{P} = \min \left[1, \frac{\mathcal{L}(\mathbf{m}')}{\mathcal{L}(\mathbf{m})} \right] \quad (8)$$

250 3. If \mathbf{m}' is accepted then it becomes the current joint model, otherwise the current state
 251 remains \mathbf{m} .

252 4. Return to point 1 above and reiterate.

253 This algorithm is capable of sampling the model space with a sampling density propor-
 254 tional to the given probability density without excessively sampling low-probability areas
 255 of the model space. This is particularly important when we consider high-dimensional
 256 model spaces in which a large proportion of the volume may have near-zero probability
 257 density.

258 Single realizations such as the mean, median or maximum likelihood model as a means
 259 of studying the solution to the general inverse problem are generally inadequate descrip-
 260 tors and are best replaced by looking at samples from the posterior *pdf*, for example.
 261 Another possibility is to calculate resolution measures, which are easily evaluated from
 262 [e.g. *Mosegaard*, 1998]

$$\mathcal{R}(\Omega, h) = \int_{\Omega} h(\mathbf{m})\sigma(\mathbf{m})d\mathbf{m} \approx \frac{1}{N} \sum_{\{n|\mathbf{m}_n \in \Omega\}} h(\mathbf{m}_n) \quad (9)$$

where $h(\mathbf{m})$ is a given function of the model parameters \mathbf{m} , Ω is an event or subset of the model space containing the models of current interest and N is the total number of samples taken from Ω . The point to note is that within the Bayesian framework we can pose any question of the sort: what is the probability for observing a given model feature ? There are generally no ill-posed questions, but just questions that have a probabilistic answer given by eq. 9.

An alternative means to quantitatively analyze the posterior *pdf* involves the standard Bayesian approach to hypothesis testing in the form of the Bayes factor, which summarizes the evidence for one hypothesis over another. The Bayes factor \mathcal{B}_{ij} for hypothesis (or model) A_i against hypothesis A_j , given data and prior information, is defined as the ratio of posterior to prior odds, or equivalently, as the ratio of likelihoods, signaling the effect of data on gauging relative prior beliefs into relative posterior beliefs [e.g. *Bernardo & Smith, 1994; Khan et al., 2004*]

$$\mathcal{B}_{ij} = \frac{\mathcal{L}(A_i)}{\mathcal{L}(A_j)} \quad (10)$$

In the following we will briefly enumerate prior information and likelihood function.

4.1. Prior Model Parameter Information

The parameters detailed below define the model parameters that describe the radial parameterization beneath the center of each pixel.

4.1.1. Crustal structure

Crustal structure is described by the physical parameters: ρ , V_p , V_s and depth to Moho. For each pixel an average four-layer crustal profile was extracted as starting model from the global crustal model CRUST2.0 (<http://mahi.ucsd.edu/Gabi/rem.html>). In each of

the four layers ρ , V_p and V_s are variable within upper and lower bounds, where the former are $\rho=1.5 \text{ g/cm}^3$, $V_p=2.5 \text{ km/s}$ and $V_s=1.5 \text{ km/s}$ and the latter correspond to the thermodynamically-determined parameter at the first depth node in the mantle, respectively. We assume additionally ρ , V_p and V_s to be non-decreasing as a function of depth, while Moho depth d_{cr} varies to within $\pm 5 \text{ km}$ (oceanic regions) and $\pm 20 \text{ km}$ (continental regions) of the crustal thickness of each pixel extracted from CRUST2.0. [13 parameters].

4.1.2. Temperature

Temperature T is assumed uniformly distributed with no lower or upper bounds, with the constraint that it be non-decreasing as a function of depth. Surface temperature is held constant at 0°C . Temperatures are specified in 25 uniform layers at intervals of 50 km in the depth range 0-700 km, and increasing to 100 km in the range from 700-2886 km. [25 parameters].

4.1.3. Compositional layer thickness

We model crust and mantle as consisting of three layers corresponding to a compositional division into crust, upper and lower mantle, respectively. Depths of these layers are located at the physically-determined Moho depth (see section 4.1.1 above), 660 and 2900 km depth, respectively. For purposes of simplification, only the '660-km' discontinuity is considered variable. Earth's surface and core-mantle-boundary (CMB) are fixed in accordance with values taken from PREM at 0 km and 2891 km depth, respectively. [1 parameter].

4.1.4. Silicate mantle composition

Mantle compositions were explored within the NCFMAS system, a model that accounts for more than 98% of mass of the mantle [Irfune, 1994]. Mantle compositions c adopted

306 here are assumed to be uniformly distributed in all four mantle layers within the bounds
 307 given in table ???. The bounds chosen for the upper mantle are such that our compositions
 308 are in agreement with the range of compositions of mantle peridotites derived from several
 309 geochemical studies (see table 2 of *Lyubetskaya & Korenaga* [2007]). [10 parameters].

310 4.1.5. Attenuation and anelasticity

311 Because of the few constraints that surface-wave tomographic studies are able to provide
 312 on Q , we follow our previous approach (standard procedure in surface-wave tomography
 313 is to fix attenuation structure) and compute Q according to eq. (1) by fixing $E_a=5\cdot 10^2$
 314 kJ/mol, $V_a=2.5\cdot 10^{-3}$ cm³/mol, $Q_0=1$ and $\alpha=0.2$ [*Sobolev et al.*, 1996; *Jackson et al.*,
 315 2002; *Cobden et al.*, 2008], while pressure p derives from the thermodynamic method and
 316 T is a model parameter. This approach ensures variability in Q without leading to large
 317 perturbations in anelastic velocities.

318 4.1.6. Anisotropy

319 Anisotropy parameters ξ , ϕ and η are assumed to be uniformly distributed within
 320 the bounds specified in table ??, which bracket most of the range of values of recent
 321 anisotropy estimates obtained from recent surface-wave tomography studies [e.g. *Panning*
 322 *& Romanowicz*, 2006; *Kustowski et al.*, 2008; *Visser et al.*, 2008b]. We also assume that
 323 anisotropy parameters are constant within the following fixed layer boundaries: 0-25, 26-
 324 50, 50-100, 100-150, 150-250, 250-350, 350-450, 450-600, 600-800, 800-1000, 1000-1200,
 325 1200-1400, 1400-1600, 1600-1800, 1800-2000 km depth. [45 parameters].

326 4.1.7. Isotropic and anisotropic physical properties

327 No constraints apply to any of these model parameters. All physical properties, in-
 328 cluding modal equilibrium mineralogy, are computed at 65 radial nodes (layer thickness

is 10 km in the depth range 0-100km; 30km in the depth ranges 100-370, 420-540 and
 570-630km; 5km in the depth ranges 370-420, 420-540, 630-700km; 100km at depths of
 700km and more).

4.2. Sampling the Posterior Distribution

Summarizing the model parameter setup, each pixel of our model is described by 94
 parameters that have to be determined. Once these parameters have been assigned val-
 ues, we compute modal mineralogy and physical properties in the crust and mantle as a
 function of pressure, temperature and composition from which Rayleigh and Love-wave
 dispersion curves are subsequently estimated.

In line with our previous study, we assume the L_2 -norm for modelling data misfit, which
 results in a likelihood function of the form

$$\mathcal{L}(\mathbf{m}) \propto \exp\left(- \sum_{\text{mode}} \sum_{\text{frequency}} \frac{[d_{obs}^R - d_{cal}^R(\mathbf{m})]^2}{2\sigma_R^2} - \sum_{\text{mode}} \sum_{\text{frequency}} \frac{[d_{obs}^L - d_{cal}^L(\mathbf{m})]^2}{2\sigma_L^2}\right) \quad (11)$$

where d_{obs} and $d_{cal}(\mathbf{m})$ denote observed and calculated data, respectively, superscripts
 indicate surface-wave type (R - Rayleigh, L - Love), and $\sigma_{R,L}$ uncertainty on either of
 these. With the L_2 -norm, we implicitly assume that data noise can be modeled using a
 gaussian distribution and that observational uncertainties and calculation errors between
 Rayleigh and Love-waves are independent.

Convergence of the algorithm is generally reached after about 10000 iterations and only
 after this stage is reached, i.e. when sampled models fit the observations, did we commence
 retaining samples from the posterior *pdf*. To ensure convergence of the MCMC algorithm
 in practice, we verified that the time series of all output parameters from the algorithm

348 were stationary throughout the entire sampling stage. In order to ensure adequate sam-
349 pling of the model space we sampled until no significant changes to the characteristics of
350 the posterior *pdf* were observed, in addition to recommencing the algorithm at a num-
351 ber of different places in the model space. To further ensure near-independent samples
352 an 'elapse time' (number of iterations) between retention of samples was implemented,
353 which was found to be 100 by analysing the autocorrelation function of the fluctuations
354 of the likelihood function. We sampled in all 1 million models from which ~ 10000 were
355 retained for analysis. The overall acceptance rate ranged from 35 to 40%.

356 The posterior probabilities so calculated are mathematical entities based on the quanti-
357 tative information used as input in the inversion. Stated differently, the probabilities are
358 based entirely on (1) data and their uncertainties, (2) prior information as quantified here
359 and (3) the physical law connecting data and unknown model parameters. In relation to
360 point (2), we have to be aware of the limitations imposed by our choice of model param-
361 eterization, as any inverse problem faces a trade-off between model parameter resolution
362 and uncertainty. No exhaustive examination of the effect of different parameterizations
363 were attempted, except for the investigation of two different compositional parameteri-
364 zations - a seven-layer model in addition to the one described here. Apart from small
365 differences in composition, all other inverted parameters were found to agree remarkably
366 within uncertainties. In summary, there is no unique way of parameterizing a model
367 system and the results simply reflect the particular parameterization chosen. Also, with
368 regard to model parameter uncertainties obtained here, we would like to note that we have
369 not considered uncertainties related to mineral physics parameters and thermodynamic
370 formulation as a result of which the model parameter uncertainties in reality are larger

371 than they appear here.

372 Given that the posterior *pdf* is defined as the conjunction of the prior with the likeli-
373 hood function (eq. 7), which are generally complex functions, the posterior *pdf* will also
374 be complex. Typically, it will be multimodal, i.e. there are many possible solutions (sec-
375 ondary extrema) in addition to the most probable solution (global extremum). In order
376 to summarize information from such a complex *pdf* standard resolution measures such as
377 means and covariances are inadequate and we have to resort to a more general approach,
378 which will typically depend on the questions that we are trying to address.

379 One-dimensional (1D) marginals are appropriate for obtaining information on single
380 parameters and their uncertainties. Information concerning other parameters, however, is
381 absent. For this, 2D or 3D marginal *pdf*'s are required, since these reveal the correlation
382 that exists among several parameters. However, of most importance here is the use of the
383 movie strategy of *Mosegaard & Tarantola* [1995] and *Tarantola* [2005], which is ideally
384 suited for analysis of the seismic tomography problem. The main point is to display a
385 collection of models taken randomly from the prior and posterior *pdfs*. This collection of
386 prior and posterior models provide us with an approximate idea of the prior information
387 used, but also, by comparison of the two, the information contained in the data. Gen-
388 eral features characteristic of the models, like those that are well-resolved, will tend to
389 be recurring in the posterior images, whereas those that are ill-resolved appear much
390 more scattered and resemble prior images. The point being that data-related structural
391 patterns are easily separable from those that appear randomly in a non-coherent and non-
392 recurring fashion. Although posterior models can differ significantly, they are nonetheless
393 models with high likelihood values that predict observed data within uncertainties (see

394 figure 2 for an example of datafit at two distinct locations). It is also the reason why the
 395 mean of such a collection of models, which itself is necessarily smooth, is *a posteriori* very
 396 unlikely as it most probably cannot fit data.

397

5. Results - Prior and posterior movies

5.1. Mantle temperature and composition

398 We start this section by showing samples from the prior *pdf*. However, rather than
 399 considering the full joint prior, we limit ourselves in this section to the fundamental pa-
 400 rameters c (here in the form of Mg#) and T . The prior models displayed in figure 3 (plots
 401 1-24) are thus samples from $f_p(\mathbf{m}_p)$ and constitute 6 thermal models picked at random at
 402 different depths in the mantle (100, 300, 500 and 1000 km depth). In addition to showing
 403 samples from the prior *pdf*, we are also showing 1D marginal *pdfs* for a given pixel at
 404 the depths indicated above. These sets of figures depict the sort of prior information that
 405 is employed here and at the same time allows us to verify that the prior *pdf* has been
 406 sampled in accordance with expectations. Note the large model variability at all depths
 407 in accordance with the few prior constraints imposed on parameters T and c (for prior
 408 information concerning the latter parameter see figure 5). Particular characteristics of
 409 these prior maps are the non-coherent and non-recurring small-scale features that vary
 410 randomly across the images as expected.

411 For comparison, figure 4 shows 6 thermal models picked randomly from the posterior
 412 *pdf* (plots 1-24) as well as 1D marginal *pdfs* at the same depths as above. The juxtapo-
 413 sition reveals the following: 1) the randomly varying pattern seen in the prior T maps
 414 has instead been replaced by coherent and repetitive structures and 2) comparison of

415 prior and posterior 1D marginal *pdfs* shows that the latter have decreased significantly in
416 width. For example, at 1000 km depth prior thermal models range from ~ 1500 to ~ 2300
417 $^{\circ}\text{C}$, whereas posterior models are confined to the range ~ 1575 - 1725 $^{\circ}\text{C}$. Both points argue
418 for well-resolved mantle temperatures.

419 Returning to the upper mantle, we clearly observe thermal variations that correlate well
420 with major geological surface features. In particular, the thermal models of the North
421 American continent reveal a strong continental contrast, dividing the tectonically active
422 western region from the tectonically stable eastern region. At 100 km depth, we find the
423 coldest parts to extend across the eastern old continental region, while the hot parts com-
424 prise the western margin and Pacific Ocean (East Pacific Rise). Cold anomalies are also
425 associated with the older (150-160 Ma) parts of the atlantic lithosphere off the southeast
426 coasts of North America, while some of the coldest anomalies are observed over the North
427 American craton. At 300 km depth, the picture described above has changed slightly
428 with the coldest anomalies centered somewhat more closely around the North American
429 craton and the East Pacific Rise remaining the hottest anomaly. Also, the lithosphere
430 beneath the southern part of NA as well as the old atlantic lithosphere to the southeast
431 have increased significantly in temperature.

432 Thermal anomaly maps of the upper mantle of NA have also been obtained by *Godey*
433 *et al.* [2004] and *Goes & Van der Lee* [2002] from inversion of a shear-wave velocity and
434 density model of North America. In spite of data and modelling differences, their thermal
435 maps at 100 and 250 km depth are found to qualitatively agree with ours, in particular
436 as concerns the thermal division of the NA continent with surface tectonic provinces.
437 Similar observations of the thermal structure of the lithosphere and upper mantle have

438 been made in a number of geophysical studies [e.g. *Jaupart & Mareschal*, 1999; *Röhm et al.*,
439 2002; *Shapiro & Ritzwoller*, 2004; *Ritzwoller et al.*, 2004; *McKenzie et al.*, 2005; *Goes et*
440 *al.*, 2005; *Faul & Jackson*, 2005; *Priestley & McKenzie*, 2006; *Kuskov et al.*, 2006, 2011;
441 *Artemieva*, 2006, 2009; *Afonso et al.*, 2008; *Simmons et al.*, 2009].

442 In the TZ, the thermal anomalies have become reversed with the NA craton now being
443 hotter than surrounding mantle, whereas the East Pacific Rise and western margin appear
444 as the coldest parts. In the lower mantle at 1000 km depth strong thermal anomalies are
445 less prevalent (amplitudes of observed thermal anomalies decrease from ~ 300 °C at 100
446 km depth to ~ 100 °C at 1000 km depth), in line with observations from seismic tomog-
447 raphy studies (see section 5.2 for more discussion) that show the largest lateral variations
448 in properties to be concentrated in the upper mantle.

449 Turning to the compositional results, we find that comparison of prior (figure 5) and
450 posterior (figure 6) models of Mg#, and particularly the 1D marginal *pdfs*, generally re-
451 veal the same behaviour discussed above for mantle *T*. In addition, the multimodel nature
452 of the 1D compositional posterior *pdf* in the upper mantle is also discernible. General
453 features of the Mg# maps seem to follow the tectonic division observed in the case of the
454 thermal maps. In particular, the old stable continental region is found to be depleted in
455 FeO (high Mg#), whereas younger continental areas and Pacific Ocean are observed to
456 be enriched in FeO. This pattern was also observed in our previous study [*Khan et al.*,
457 2010] and had been hypothesized by e.g. *Jordan* [1975, 1978] as a means of explaining the
458 stability of continental roots. Further evidence for compositional variations of the conti-
459 nental lithosphere also come from a number of geochemical analyses of mantle xenoliths
460 and cratonic peridotites [e.g. *Boyd*, 1989; *Rudnick et al.*, 1998; *Griffin et al.*, 1999; *Gaul*

461 *et al.*, 2000; Artemieva, 2009; Afonso *et al.*, 2010].

462 With the present simplified mantle compositional parameterization, no compositional
463 variations in the TZ are observed. In the lower mantle, we find, as in the case of mantle
464 temperatures, composition to vary relatively little laterally. Mg# anomalies are seen to
465 vary between 0.9 and 0.92, implying general Fe-depletion. Overall, there is a noticeable
466 tendency for higher Mg# in the lower mantle relative to the upper mantle, suggesting
467 compositional differences between the two as observed in our previous study [*Khan et al.*,
468 2010].

469 With regard to possible trade-offs between c and T , figure 7 shows plots of 2D marginal
470 posterior *pdf*'s for the latter parameters in the upper and lower mantle, which reveal
471 no noticeable correlation. However, given different depth parameterizations for the two
472 parameters, the correlations here represent a temperature average over the layers that
473 bracket the two compositional layers.

474 Finally, we would like to note that our thermo-chemical results presented here are based
475 on the assumption of thermodynamic equilibrium. *Xu et al.* [2008] have discussed a pos-
476 sible alternative, the mechanical mixture model. From the point of view of geophysics
477 there is no argument for or against either model. However, from a petrological viewpoint
478 it can be argued that while the mechanical mixture model plausibly depicts the influence
479 of chemical segregation on the equilibrium model, it cannot be claimed to be a more
480 realistic endmember for the earth's mantle because it is inconsistent with mid-ocean ridge
481 volcanism (for more discussion see *Khan et al.*, 2009).

482

5.2. Isotropic shear-wave velocity structure

483 Posterior movies (for brevity we omit prior movie) of mantle shear-wave velocity struc-
 484 ture are shown in figure 8. For comparison, we have also included two regional seismic
 485 tomography models: the anisotropic shear-wave velocity models of North America by
 486 *Nettles & Dziewonski* [2008] and *Yuan et al.* [2011]. The model by *Nettles & Dziewonski*
 487 (henceforth ND08) is based on a large number of global and regional measurements of the
 488 dispersion of fundamental-mode surface-waves. The model of *Yuan et al.* (YU11) was ob-
 489 tained from inversion of long-period fundamental-mode and overtone surface-waveforms.
 490 Model ND08 is restricted to the upper mantle, while model YU11 has some sensitivity in
 491 the upper TZ. Thus no comparison with previous models is made in the lower mantle.

492 Structural features in the posterior movies (figure 8, plots 1-24), repeat across the differ-
 493 ent images, implying a well-resolved *S*-wave velocity structure, particularly in the upper
 494 mantle and TZ. The main continental division so clearly apparent in the posterior thermal
 495 and compositional movies, is closely followed here at 100 km depth. The old eastern parts
 496 of the NA continent that were found to be cold and Fe-depleted appear as regions of fast
 497 *S*-wave velocity, while the younger and hotter, Fe-enriched regions (the western margin
 498 and Pacific Ocean) are observed to be relatively slow. The division between the tecton-
 499 ically active and tectonically stable parts of NA is seen to follow the Rocky Mountain
 500 front as first outlined by *Grand* [1994]. These features are also clearly apparent at the
 501 same depth in models ND08 and YU11 (see figure 8) as well as in many regional seismic
 502 surface-wave and travel-time tomography models of NA [e.g. *Van der Lee & Nolet*, 1997b;
 503 *Frederiksen et al.*, 2001; *Li et al.*, 2002; *Godey et al.*, 2004; *Van der Lee & Frederiksen*,
 504 2005; *Sigloch et al.*, 2008] and many other fundamental-mode global seismic surface-wave

505 tomography models [e.g. *Ekström et al.*, 1997; *Trampert & Woodhouse*, 2001; *Shapiro &*
506 *Ritzwoller*, 2002; *Lebedev & Van der Hilst*, 2008].

507 At 300 km depth the ocean-continent contrast is still discernible (figure 8, plots 7-12),
508 with the oldest stable part of the continent appearing to be somewhat faster than sur-
509 rounding mantle, while the region centered on the NA craton is characterized by being
510 distinctly faster. These features can also be perceived in ND08 and YU11. Fast S -wave
511 velocity anomalies around the NA craton are found to persist down to ~ 300 km depth
512 in all models shown here. This is further supported by the shear-wave velocity profiles
513 shown in figure 9. From 300 km depth and deeper differences in S -wave velocities beneath
514 the various tectonic settings disappear as a result of which this part of the upper mantle
515 appears more homogeneous.

516 In the TZ (figure 8, plots 13-18) we observe a much smoother picture with peak-to-peak
517 velocity variations being ~ 0.1 km/s, in comparison to the upper mantle where variations
518 ranged from 0.2 to 0.3 km/s. This is also evident from figure 9, which indicates that
519 the TZ is less heterogeneous than the upper mantle. Velocities are also found (figure 8,
520 plots 13-18) to have reversed with the older continental parts now being characterized by
521 slower velocities relative to younger areas. This reversal is also observed in model YU11
522 and features in several seismic tomography studies [e.g. *Ritsema et al.*, 2004; *Panning &*
523 *Romanowicz*, 2006; *Visser et al.*, 2008a; *Kustowski et al.*, 2008; *Lebedev & Van der Hilst*,
524 2008].

525 In the lower mantle at 1000 km depth (figure 8, plots 19-24), lateral velocity variations
526 are now < 0.1 km/s, implying a much more homogeneous lower mantle relative to the up-
527 per mantle. Note also the general overlap of S -wave velocity profiles in figure 9 for depths

528 > 700 km. This observation is also common among global S -wave tomography models,
529 which are typically characterized by an absence of strong heterogeneities at long wave-
530 lengths below 650 km depth, resulting in a spectrally white distribution of mid-mantle
531 isotropic shear-wave velocity anomalies [e.g. *Ritsema et al.*, 2004; *Panning & Romanow-*
532 *icz*, 2006; *Kustowski et al.*, 2008].

533 Comparing our models with previous regional seismic tomography models shows a high
534 degree of correlation in the upper mantle, amplitudes aside. This level of agreement is
535 indeed reassuring given the fundamentally different approach employed here to inverting
536 seismic data. The problem with amplitudes of retrieved velocity anomalies is a well-known
537 and persistent feature of all seismic tomography models and is mostly related to the use
538 of different regularization schemes/damping parameters and choice of particular 1D ref-
539 erence model. In addition to this, discrepancies between tomography models are known
540 to arise around the TZ, where the correlation coefficient between various global tomog-
541 raphy models is found to decrease strongly [e.g. *Kustowski et al.*, 2008]. On the face of
542 it such discrepancies are also palpable here at e.g. 500 km depth (compare plots 13-18
543 with model YU11. Yuan et al. find a large low-velocity province beneath central North
544 America that is not imaged to the same extent in our maps, which could be interpreted
545 as an inconsistency of our data set and the measurements of Yuan et al. However, a
546 closer look at sampled velocities at 500 km depth beneath several pixels in the form of
547 1D marginal *pdf*'s (figure 10) reveals a considerable degree of consistency inasmuch as
548 model YU11 generally lies within the range of presently sampled shear-wave velocities.
549 In addition, if uncertainty estimates for model YU11 could be taken into account any
550 remaining discrepancies would most likely disappear (pers. comm. H. Yuan, 2011). Note

551 that the marginal 1D *pdf*'s appear gaussian, whereby the mean shear-wave velocity (\bar{V}_S)
 552 and its standard deviation (σ_{V_S}) can be computed. Maps of \bar{V}_S and $\bar{V}_S \pm \sigma_{V_S}$ are shown
 553 as online supporting material figure S1.

554 We have so far abstained from discussing mantle attenuation structure because it is
 555 less well-constrained. The latter is a result of the large uncertainties that exist on the
 556 attenuation-related parameters Q_o , V_a , E_a and α that are employed here for calculating
 557 attenuation structure. However, we made several tests, where we varied the aforemen-
 558 tioned parameters by as much as 10-20%, to verify that the results did not change.

559 Given the fundamental approach of inverting directly for c and T , we also constrain
 560 P -wave velocity and density. However, for reasons of brevity these results are not shown
 561 here, but can be found as online supporting material (see online supporting figures S2-S3).

5.3. Anisotropic shear-wave velocity structure

562 Prior and posterior anisotropic shear-wave velocity models are shown in figures 11 -
 563 12, and as in the case of S -wave velocity structure, model features appear fairly robust
 564 across much of the mantle shown here. At 100 km depth (figure 12, plots 1-6), most of
 565 the Pacific Ocean and NA continent are characterized by positive anisotropic anomalies
 566 ($\xi > 1$), in agreement with what is seen in the previous regional tomographic models
 567 ND08 and YU11. At a depth of 150 km (for brevity images at intermediate depths are
 568 not shown) these features persist across all models, except for the tectonically young areas
 569 centered on the west coast, for which $\xi < 1$ now. This pattern is reinforced at 200 km
 570 depth, with all parts of the western margin, the southeast and a large part of the Pacific
 571 Ocean having $\xi < 1$, i.e. $V_{sv} > V_{sh}$ as can be seen from figure 12 (plots 7-12) at 300 km
 572 depth. This largely tectonically-driven signal is seen to extend to 350 km depth here (not

shown), with old stable continental areas characterized by $\xi > 1$, in contrast to younger regions where $\xi < 1$. Parts of these features recur to some extent in ND08 and YU11.

The upper mantle anisotropy structure retrieved here generally agrees with the global anisotropic tomography model of *Gung et al.* [2003], who found the East Pacific Rise, western margin and southeastern part of NA to be characterized by $\xi < 1$, while for the stable continental regions $\xi > 1$. In particular, they observed that at 300 km depth, the roots of most cratons were characterized by $\xi > 1$, which extend down to 400 km depth, whereas for the East Pacific Rise $\xi < 1$ down to 300 km depth.

As we cross into the TZ a general change in anisotropic signal is observed that mimicks the reversal in isotropic shear-wave velocity pattern observed in the maps shown earlier (see figure 8, plots 13-18). This change commences around 400 km depth and grows more coherent as we transcend deeper into the TZ. In particular, the area centered on the NA craton and eastern part of NA as well as East Pacific Rise are regions where negative ξ anomalies predominate, i.e. $V_{sv} > V_{sh}$. In the lower mantle another subtle change in anisotropy occurs and most of the lower mantle appears to be relatively homogeneous, characterized by predominantly positive anisotropy anomalies.

The question of anisotropy in and below the TZ has been studied for some time now [e.g. *Montagner & Kennett*, 1996; *Trampert & Van Heijst*, 2002; *Wookey et al.*, 2002; *Panning & Romanowicz*, 2006; *Visser et al.*, 2008b; *Kustowski et al.*, 2008], although little agreement has emerged. *Kustowski et al.* [2008], for example, correlated their whole-mantle anisotropic model S362WANI with the one derived by *Panning & Romanowicz* [2006] SAW642AN and found anisotropic variations only to be consistent in the upper-most (150 km) and lower-most mantle (2800 km). Our model comparisons here support

596 the contention that anisotropic models generally only agree in the upper-most mantle.

597 To further investigate the robustness of the TZ and lower mantle anisotropy signal
598 retrieved here (figure 12, plots 13-24), we analyzed the correlation between ξ and all
599 other parameters that might potentially be interfering, such as c , T and V_s . However, no
600 trade-offs were observed (not shown for brevity), as expected. Additionally, we looked at
601 shear-wave anisotropy maps at 1800 km depth and found prior (figure 11, plots 25-30) and
602 posterior (figure 12, plots 25-30) movies to be similar in character with small-scale features
603 varying randomly across the maps, typical of all prior plots shown hitherto. Again, this
604 follows our expectation, inasmuch as the surface-wave data only have sensitivity to ~ 1300
605 km depth. This suggests that the structural patterns seen at 1000 km depth are data-
606 related as these are easily separable from those that appear randomly in a non-coherent
607 and non-recurring fashion, as pointed out previously.

608 Anisotropy plays an important role in seismic tomography, because of the potential
609 constraints that it provides on mantle flow. Anisotropy is thought to be an indicator of
610 present-day mantle strain field or past deformation frozen in the lithosphere [e.g. *Tanimoto*
611 *& Anderson*, 1984; *Montagner & Tanimoto*, 1991; *Karato*, 1998; *Montagner*, 1998; *Becker*
612 *et al.*, 2008; *Long & Becker*, 2010]. Changes in sign of anisotropy can thus be interpreted as
613 indicating changes from horizontal to vertical flow under the assumption that anisotropy
614 is the result of a preferred orientation of the crystal lattice of the anisotropic mantle
615 minerals as these are subjected to strains due to mantle flow. With this in mind, our
616 results suggest a prevailing horizontal shear flow in the asthenosphere beneath continents,
617 while the reverse is the case beneath oceanic regions and likely also younger continental
618 areas. Several changes in sign of anisotropy are observed here, that might be indicative of

619 the presence of a number of distinct anisotropic layers for the lithosphere, asthenosphere,
 620 TZ and possibly lower mantle. A division of the upper mantle beneath NA into distinct
 621 anisotropic lithospheric and asthenospheric layers has been proposed earlier by *Gaherty*
 622 [2004], *Marone et al.* [2007], *Deschamps et al.* [2008] and *Yuan et al.* [2011], as well as
 623 other cratonic areas in general [*Debayle et al.*, 2005].

624 So far we have exclusively discussed shear-wave anisotropy, leaving the other anisotropy
 625 parameters, i.e. ϕ and η , aside. P -wave anisotropy has been studied by e.g. *Anderson &*
 626 *Dziewonski* [1982], *Boschi & Dziewonski* [2000] and *Beghein & Trampert* [2003], although
 627 as in the case of S -wave anisotropy in the TZ and lower mantle consensus is yet to emerge,
 628 which is due to the limited sensitivity of the surface-wave data to P -wave anisotropy. As
 629 a result global seismic tomography studies simply scale P to S -wave anisotropy [e.g.
 630 *Panning & Romanowicz*, 2006; *Kustowski et al.*, 2008; *Visser et al.*, 2008a,b]. Although
 631 we have taken a somewhat more lenient approach in that we also inverted for ϕ , we will
 632 not discuss the results in any detail, given that ϕ is less well-constrained. The same
 633 arguments apply to η . However, we did verify that our particular parameterization did
 634 not lead to perturbation of the radial shear-wave anisotropic signal found here.

6. Posterior filtering of tomographic models using geoid anomalies

635 Additional geophysical data can be employed as a tool to refine and narrow the collection
 636 of tomographic models. As auxiliary geophysical data we consider geoid anomalies, since
 637 these are directly related to the density structure.

638 A major difficulty with modeling geoid anomalies from a prescribed density distribution
 639 is to correctly estimate the dynamic contribution to the geoid anomalies [e.g., *Ricard et*
 640 *al.*, 1984; *Forte and Peltier*, 1987; *Hager & Richards*, 1989]. Furthermore, reconstructing

641 geoid anomalies from regional models that are not developed in spherical harmonics,
 642 requires 1) prescribing an appropriate band-pass window and 2) accounting for lateral
 643 density distributions [Kogan & McNutt, 1993]. Here, we compute geoid anomalies δN
 644 for the six density models shown in the posterior movie (see online supporting material,
 645 figure S4) following the regional approach described in van Gerven *et al.* [2004],

$$\delta N(\theta, \phi) = \frac{3}{4\pi\rho_m} \int_{r_{\text{CMB}}}^R \int_0^{2\pi} \int_{-\pi/2}^{\pi/2} K_g(\Delta, r) \delta\rho(r, \theta', \phi') \sin\theta' d\theta' d\phi' dr \quad (12)$$

646 where ρ_m , R and r_{CMB} are Earth's mean density, surface and core radius, respectively and
 647 Δ angular distance between the point where the geoid is measured (θ, ϕ) and the location
 648 of the density anomaly (θ', ϕ') . The local geoid kernels $K_g(\Delta, r)$ describe the response of
 649 the geoid to a density anomaly located at the position (r, θ', ϕ') in the band-pass filter
 650 $l_1 \leq l \leq l_2$ and are given by

$$K_g(\Delta, r) = \sum_{l=l_1}^{l_2} G_l(r) P_l^0(\cos \Delta) \quad (13)$$

651 where $P_l^0(\cos \Delta)$ and $G_l(r)$ are Legendre Polynomials and radial geoid kernels, respec-
 652 tively. We calculated the radial kernels using the method of Forte [2000], which assumes
 653 viscosity to vary radially. It should also be noted that the radial geoid kernels depend
 654 strongly on the choice of viscosity profile, although this becomes less important with in-
 655 creasing spherical harmonic degree. To compute geoid anomalies from eq. (12) requires
 656 an appropriate viscosity profile, a cut-off angular distance Δ_c and a spherical harmonic
 657 band-pass filter.

658 For each pixel of our posterior models viscosity profiles for the upper mantle were calcu-
 659 lated in a consistent manner as a function of temperature and pressure following Korenaga
 660 & Karato [2008]. From these, we define two viscosity models, 1) a continental average

661 where all viscosity profiles have been averaged over the entire study area (henceforth
 662 model CAV) and 2) a tectonic average (model RAV) where viscosity profiles are averaged
 663 within four tectonically distinct regions (labeled s, q, p and r in *Khan et al.* [2011] and cor-
 664 responding to the North American craton, stable platforms, tectonically active areas, and
 665 surrounding oceans, respectively). For model RAV geoid kernels were computed for each
 666 tectonic viscosity profile, which implies that the radial geoid kernels in eq. (13) depend
 667 implicitly on the angular distance ($G_l(r, \Delta)$). In the lower mantle (for depths >1200 km),
 668 where our thermo-chemical distributions are less well-constrained, we employ the recent
 669 viscosity model of *Soldati et al.* [2009], which was obtained by inverting global gravity
 670 data (GRACE). Additionally, at 660 km depth a viscosity ratio of 30 was imposed. The
 671 viscosity models so computed are shown in figure S4 (online supporting material). Note
 672 that in the case of the regionally averaged viscosity model (Figure S5b), most of the dis-
 673 crepancy between the different tectonic regions appears in the depth range 100-500 km.

674 Amplitudes of local geoid kernels rapidly decrease with angular distance even in the
 675 case of small values ($<20^\circ$) of the cut-off angular distance Δ_c . here, we fixed Δ_c at 60° ,
 676 which is sufficient for present purposes. We also tested other values of Δ_c , but did not
 677 observe any significant changes in the computed geoid for $\Delta_c >25^\circ$.

678 As upper (l_2) and lower (l_1) bounds on the band-pass filter, we set $l_1=6$ and $l_2=20$,
 679 respectively. Low spherical harmonic degrees (<5) mostly sample the deep (>1000 km)
 680 mantle (online supporting material figure S5), and can thus safely be discarded. In con-
 681 trast, degrees $l >10$ are mostly sensitive to the upper mantle. Presently, we limited
 682 our expansion to $l_2=20$ to account for the fact that small-scale anomalies may be less
 683 well-resolved. Intermediate ($6 \leq l \leq 9$) degrees sample both the upper and lower mantle.

684 Keeping this intermediate range is thus likely to introduce a deep-mantle signal. On the
685 other hand, removing this range would discard continental-scale variations that originate
686 in the upper mantle, which likely introduces a stronger bias.

687 In Figure 13, we plotted the geoid anomalies (filtered in the band-pass $6 \leq l \leq 20$)
688 predicted from our six posterior density models together with the geoid anomalies from
689 model GGM02 [Tapley *et al.*, 2005] (plot A), which is based on GRACE data. Plots 1-6
690 were obtained with viscosity profile CAV discussed previously, whereas plots 7-12 were
691 constructed using RAV viscosity profile. Observed geoid anomalies (plot A) show a clear
692 continental division, with geoid lows (down to -30 m) in the north-east, and geoid highs
693 (up to 30 m) along the Rocky Mountains and the Basin and Range. Geoid highs (lows)
694 with smaller amplitude are also present over the Central plains (adjacent Pacific Ocean).
695 Clearly, strong discrepancies exist between the geoid anomalies predicted by the different
696 posterior models, suggesting that the geoid is potentially a useful filter to refine the col-
697 lection of posterior models.

698 Overall, geoid anomalies obtained with the regionally averaged viscosity profile explain
699 the observations better. The geoid anomaly model that agrees best with GGM02 is model
700 4 (plots 4 and 10). For geoid anomalies reconstructed with the regionally averaged vis-
701 cosity profiles, correlation and variance reduction reach 0.63 and 0.40, respectively. A
702 striking discrepancy of all our geoid anomaly maps, however, is the small amplitude of
703 the geoid lows over the North American craton (around -10 m instead of -30 m in GGM02).
704 This difference may be due to the low-resolution compositional parameterization in radial
705 direction that we employed. The posterior density models may thus fail to capture the
706 entire compositional signal, which is expected to be relatively strong and to vary with

707 depth on a continental scale. Posterior models 1 (plots 1 and 7) and 2 (plots 2 and 8) also
708 correlate reasonably well with the observed geoid (correlation of 0.42), but the relatively
709 low amplitude geoid anomalies lead to poor variance reduction (0.16 and 0.10 for models
710 1 and 2, respectively). In contrast, model 6 is found to disagree strongly with GGM02
711 and may thus be removed from the collection of posterior models.

712 Testing posterior tomographic models against gravity data is a promising tool for fur-
713 ther refining tomographic models based entirely on seismic data. However, the method
714 employed here to reconstruct geoid anomalies from posterior density models suffers two
715 important limitations that should be kept in mind. First, it strongly depends on the
716 assumed radial viscosity structure, which is not well constrained. To illustrate this, we
717 conducted additional calculations, in which we used three global radial viscosity models
718 from the studies of *Ricard et al.* [1993]; *Forte & Mitrovica* [2004]; *Yoshida & Nakakuki*
719 [2009]. For all three cases, we obtained geoid anomalies that correlate to a reasonably
720 extent with GGM02 (from 0.40 to 0.60, depending on the particular viscosity model), but
721 strongly differ in amplitude, resulting in negative variance reductions. The continental
722 and regional viscosity models based on the posterior thermo-chemical distributions give
723 better results, but uncertainty and errors exist in the rheological parameters we used [*Ko-*
724 *renaga & Karato, 2008*] that are propagated to the viscosity profiles. Second, the spectral
725 method we employ here to model mantle viscous flow neglects the toroidal part of the
726 flow, i.e. lateral viscosity variations are not accounted for. Because viscosity controls the
727 dynamic topography, this may have strong implications for the geoid kernels and anoma-
728 lies. Our results suggest that the use of regional viscosity models partially compensates
729 for this neglect of the toroidal flow. Furthermore, geoid reconstructions based on a finite-

730 volume model of thermal convection that account for lateral viscosity variations, suggest
731 that the effect of lateral viscosity variations on geoid anomalies is moderate and vary with
732 location [*Cammarano et al.*, 2011]. Additional studies, including the calculation of geoid
733 kernels from finite-volume convection models, should be conducted in order to obtain
734 more detailed insights into the effect of including lateral viscosity variations.

7. Conclusion

735 The primary purpose of the present study has been to describe an alternative means
736 of inverting seismic surface-wave phase velocities and their uncertainties, through which
737 relatively robust measures of resolution and uncertainty can be obtained. Specifically, this
738 was facilitated by the use of a Markov chain Monte Carlo method that works by performing
739 a random walk in a multidimensional model space. It combines prior information with
740 information from measurements and from the theoretical relationship between data and
741 model parameters. This was effectuated using the Metropolis algorithm. As output we
742 assimilated random realizations of the posterior *pdf*, which contains all the information
743 about our parameterized physical system. We presented the outcome as a collection of
744 tomographic images that all fit data within uncertainties. The emphasis here is on drawing
745 inferences from such an assembly of models, rather than just a single image.

746 As outlined, our method also goes beyond the traditional approach of inverting seismic
747 data for seismic wave speeds, by employing a self-consistent thermodynamic technique in
748 order that the former can be inverted directly for thermo-chemical structure of the Earth's
749 mantle. The obvious advantage of inverting for a set of parameters that describe the
750 system being studied at the fundamental level of chemical composition and temperature,
751 is that all physical properties are derived from these parameters. As a result, the use

752 of simplified scaling relationships that seek to bridge the limited sensitivity of a given
753 data set with regard to other structural parameters is entirely obviated. Moreover, the
754 approach allows us to naturally link geophysical data that are not *a priori* related such
755 as seismic, gravity and electromagnetic sounding data, thus opening the avenue for joint
756 inversions across different geophysical fields.

757 To render the current study feasible, we considered phase velocity maps as data in
758 place of phase velocity measurements, from which the former are derived. As a result,
759 we inverted for a set of local 1D radial profiles spanning the North American continent
760 and parts of the adjacent Pacific Ocean. Data uncertainties derive from a model space
761 search technique to fit phase velocity measurements of fundamental-mode and higher-
762 order Rayleigh and Love waves, which is deemed to provide an adequate estimate of
763 uncertainties on the resultant phase velocity maps [*Visser et al.*, 2008a]. In spite of this,
764 we nonetheless consider the present approach successful, inasmuch as there is considerable
765 agreement between present and previous seismic shear-wave tomography models, which,
766 given the fundamentally different approaches, is considered strong evidence in support
767 of our method. Keeping in mind that we presently do not consider uncertainties on
768 thermodynamic parameters, in addition to assuming a thermodynamically equilibrated
769 mantle, we observe that

- 770 1. the North American upper mantle thermo-chemical and physical structure follows
771 the surface tectonic age-division closely,
- 772 2. the old stable continental parts were found to be cold and Fe-depleted, while the
773 tectonically younger continental regions and oceanic lithosphere appeared relatively hot
774 and Fe-enriched,

775 3. shear-wave velocity differences between oceans and continents disappeared around
776 300 km depth,

777 4. within the transition zone a decoupling of the structure (thermo-chemical and
778 anisotropic) from that of the upper mantle occurred, accompanied by an overall decrease
779 of amplitudes of velocity anomalies,

780 5. the lower mantle is characterized by an overall absence of strong heterogeneities so
781 prominent in the upper mantle, although there is evidence for compositionally distinct
782 upper and lower mantles and that

783 6. the anisotropic upper mantle structure is akin to what has been observed in some
784 previous studies, in particular a significant positive ξ signal is present beneath the old
785 stable continental part, whereas younger areas are typically characterized by negative
786 shear-wave anisotropy. In the transition zone a general reversal of the anisotropy signal
787 compared to above is observed, which seems to repeat, albeit to a lesser extent, in the
788 lower mantle at 1000 km depth. This likely reflects the presence of distinct anisotropic
789 layers in the mantle, and finally

790 7. testing posterior tomographic models using geoid anomalies, which are sensitive to
791 density, presents a promising tool for refining the collection of sampled tomographic and
792 thermo-chemical models. A current limitation, however, is the accuracy of the recon-
793 structed geoid, which requires a good knowledge of the mantle viscosity structure.

794 **Acknowledgments.** We would like to thank K. Visser and J. Trampert for distributing
795 their global surface-wave phase-velocity maps. We are also grateful to M. Nettles and H.
796 Yuan for sharing their tomography models with us. Comments by J. Ritsema on an earlier
797 manuscript were much appreciated. As were discussions with L. Boschi. This work was

798 supported by Swiss National Science Foundation grants 200021-130411 (AK) and 200021-
799 111870 (FD). We would also like to thank G. Nolet for a copy of his code computing
800 surface-wave phase velocity dispersion curves. Numerical computations were performed
801 on the ETH cluster Brutus. Figures were generally prepared using GMT (Wessel & Smith,
802 1998).

References

- 803 Afonso, J. C., M. Fernàndez, G. Ranalli, G., W. L. Griffin, J. A. D. Connolly,
804 Combined geophysical-petrological modelling of the lithospheric-sublithospheric up-
805 per mantle: methodology and applications, *Geochem. Geophys. Geosyst.*, *9*, Q05008,
806 doi:10.1029/2007GC001834, 2008.
- 807 Afonso, J.C., G. Ranalli, M. Fernàndez, W. L. Griffin, S. Y. O'Reilly & U. Faul, On the
808 Vp/Vs - Mg# correlation in mantle peridotites: Implications for the identification of
809 thermal and compositional anomalies in the upper mantle, *Earth Planet. Sci. Lett.*, *289*,
810 606, 2010.
- 811 Aki, K., A. Christoffersen & E. Husebye, Determination of the three-dimensional structure
812 of the lithosphere, *J. Geophys. Res.*, *82*, 277, 1977.
- 813 Anderson, D. L., *Theory of the Earth*, Blackwell, Oxford, 1989.
- 814 Anderson, D. L. & A. M. Dziewonski, Upper mantle anisotropy: Evidence from free
815 oscillations, *Geophys. J. R. Astron. Soc.*, *69*, 383, 1982.
- 816 Artemieva, I. M., Global 1°C×1°C thermal model TC1 for the continental lithosphere:
817 implications for lithosphere secular evolution, *Tectonophysics*, *416*, 245, 2006.

- 818 Artemieva, I. M., The continental lithosphere: Reconciling thermal, seismic and petrologic
819 data, *Lithos*, *109*, 23, 2009.
- 820 Babuska, V. & Cara, M., *Seismic anisotropy in the Earth*, Kluwer Academic Press, Boston,
821 USA, 1991.
- 822 Becker, T. W., B. Kustowski & G. Ekström, Radial seismic anisotropy as a constraint for
823 upper mantle rheology *Earth Planet. Sci. Lett.*, *267*, 213, 2008.
- 824 Beghein, C. & J. Trampert, Probability density function for radial anisotropy: implica-
825 tions for the upper 1200 km of the mantle, *Earth Planet. Sci. Lett.*, *217*, 151, 2003.
- 826 Bernardo, J. M. & A. F. M. Smith, *Bayesian Theory*, Chichester: Wiley, 1994.
- 827 Bodin, T., Sambridge, M. & Gallagher, K., A self-parameterising partition
828 model approach to tomographic inverse problems, *Inverse Problems*, *25*, 055009,
829 doi:10.1088/0266-5611/25/5/055009, 2009.
- 830 Bosch, M., Lithologic tomography: From plural geophysical data to lithology estimation,
831 *J. Geophys. Res.*, *104*, 749, 1999.
- 832 Boschi, L. & A. M. Dziewonski, high and low resolution images of the Earth's mantle -
833 Implications of different approaches to tomographic modeling, *J. Geophys. Res.*, *104*,
834 25567, 1999.
- 835 Boschi, L. & A. M. Dziewonski, Whole Earth tomography from delay times of P, PcP, PKP
836 phases: lateral heterogeneities in the outer core, or radial anisotropy in the mantle?, *J.*
837 *Geophys. Res.*, *105*, 675, 2000.
- 838 Boschi, L. & G. Ekström, New images of the Earth's upper mantle from measurements of
839 surface-wave phase velocity anomalies, *J. Geophys. Res.*, *107*, 10.1029/2000JB000059,
840 2002.

- 841 Boyd, F. R., Compositional distinction between oceanic and cratonic lithosphere, *Earth*
842 *Planet. Sci. Lett.*, *96*, 15, 1989.
- 843 Cammarano, F., B. Romanowicz, L. Stixrude, C. Lithgow-Bertelloni & W. Xu, Inferring
844 the thermochemical structure of the upper mantle from seismic data, *Geophys. J. Int.*,
845 *179*, 1169, doi: 10.1111/j.1365-246X.2009.04338.x.
- 846 Cammarano, F., P.J. Tackley, and L. Boschi, Seismic, petrological and geodynamical
847 constraints on thermal and compositional structure of the upper mantle: global thermo-
848 chemical models, *submitted to Geophys. J. Int.*, 2011.
- 849 Cobden, L., S. Goes, F. Cammarano & J. A. D. Connolly, Thermochemical interpretation
850 of one-dimensional seismic reference models for the upper mantle: evidence for bias due
851 to heterogeneity, *Geophys. J. Int.*, *175*, 627, 2008.
- 852 Connolly, J. A. D., Computation of phase equilibria by linear programming: A tool for geo-
853 dynamic modeling and an application to subduction zone decarbonation, *Earth Planet.*
854 *Sci. Lett.*, *236*, 524, 2005.
- 855 Debayle, E., B. L. N. Kennett & K. Priestley, Global azimuthal seismic anisotropy and
856 the unique plate-motion deformation of Australia, *Nature*, *433*, 509, 2005.
- 857 Deschamps, F., R. Snieder & J. Trampert, The relative density-to-shear velocity scaling
858 in the uppermost mantle, *Phys. Earth Planet. Int.*, *124*, 193, 2001.
- 859 Deschamps, F. & J. Trampert, Mantle tomography and its relation to temperature and
860 composition, *Phys. Earth Planet. Int.*, *140*, 277-291, 2003.
- 861 Deschamps, F., S. Lebedev, T. Meier & J. Trampert, Stratified seismic anisotropy reveals
862 past and present deformation beneath the East-central United States, *Earth Planet.*
863 *Sci. Lett.*, *274*, 489, doi: 10.1016/j.epsl.2008.07.058, 2008.

- 864 Dziewonski, A. M. & D. L. Anderson, Preliminary reference Earth model, *Phys. Earth*
865 *Planet. Int.*, *25*, 297, 1981.
- 866 Dziewonski, A. M., B. H. Hager & R. J. O'Connell, Large-scale heterogeneity in the lower
867 mantle, *J. Geophys. Res.*, *82*, 239, 1977.
- 868 Ekström, G., J. Tromp & E. W. F. Larson, Measurements and global models of surface
869 wave propagation, *J. Geophys. Res.*, *102*, 8137, 1997.
- 870 Ekström, G. & A. M. Dziewonski, The unique anisotropy of the Pacific upper mantle,
871 *Nature*, *394*, 168, 1998.
- 872 Forte, A.M., Seismic-geodynamic constraints on mantle flow: implications for layered
873 convection, mantle viscosity, and seismic anisotropy in the deep mantle, in S.-I. Karato
874 et al. (Eds), Earth's deep interior: mineral physics and tomography from the atomic
875 to the global scale, *Geophysical Monograph Ser.*, **117**, American Geophysical Union,
876 Washington, DC, pp. 3-36, 2000.
- 877 Forte, A.M. and W.R. Peltier, Plate tectonics and aspherical Earth's structure: the im-
878 portance of poloidal-toroidal coupling, *J. Geophys. Res.*, *92*, 3645, 1987.
- 879 Faul, U.H. & I. Jackson, The seismological signature of temperature and grain size vari-
880 ations in the upper mantle, *Earth Planet. Sci. Lett.*, *234*, 119, 2005.
- 881 Frederiksen, A. W., M. G. Bostock & J. F. Cassidy, *S* wave velocity structure of the
882 Canadian upper mantle, *Phys. Earth Planet. Int.*, *124*, 175, 2001.
- 883 Gaherty, J., A surface wave analysis of seismic anisotropy beneath eastern North America,
884 *Geophys. J. Int.*, *158*, 1053, 2004.
- 885 Gaul, O. F., W. L. Griffin, S. Y. O'Reilly & N. J. Pearson, Mapping olivine composition
886 in the lithospheric mantle, *Earth Planet. Sci. Lett.*, *182*, 223, 2000.

- 887 Godey, S., F. Deschamps F., J. Trampert & R. Snieder, Thermal and compositional
888 anomalies beneath the North American continent, *J. Geophys. Res.*, *109*, B01308, doi:
889 10.1029/2002JB002263, 2004.
- 890 Goes, S. & S. van der Lee, Thermal structure of the North American uppermost mantle
891 inferred from seismic tomography, *J. Geophys. Res.*, *107*, 11153, 2002.
- 892 Goes, S., F. J. Simons & K. Yoshizawa, Seismic constraints on temperature of the Aus-
893 tralian uppermost mantle, *Earth Planet. Sci. Lett.*, *236*, 227, 2005.
- 894 Grand, S. P., Mantle shear structure beneath the americas and surrounding oceans, *J.*
895 *Geophys. Res.*, *99*, 11591, 1994.
- 896 Grand, S. P., R. D. Van der Hilst & S. Widiyantoro, *GSA Today*, *7*, 1, 1997.
- 897 Griffin, W. L et al., Layered mantle lithosphere in the Lac du Gras Area, Slave Craton:
898 Composition, structure and origin, *J. Petrol.*, *40*, 705, 1999.
- 899 Gung, Y, M. Panning & B. Romanowicz, Global anisotropy and the thickness of conti-
900 nents, *Nature*, *442*, 707, 2003.
- 901 Hager, B.H., and M.A. Richards, Long wavelength variations in Earth's geoid: physical
902 models and dynamical implications, *Philos. Trans. R. Soc. Lon. A*, *328*, 309-327.
- 903 Hastings, W. K., Monte Carlo sampling methods using Markov chains and their applica-
904 tions, *Biometrika*, *57*, 97, 1970.
- 905 Irifune, T., Absence Of An Aluminous Phase In The Upper Part Of The Earths Lower
906 Mantle, *Nature*, *370*, 131, 1994.
- 907 Jackson, I., Laboratory Measurements of Seismic Wave dispersion and Attenuation: Re-
908 cent Progress, in *Earth's Deep Interior: Mineral Physics and Tomography from the*
909 *Atomic to the Global Scale*, Geophys. Monogr. Ser., vol. 117, eds. S. Karato et al.,

- 910 AGU, Washington, D. C., 265, 2000.
- 911 Jackson, I., J. D. Fitz Gerald, U. H. Faul & B. H. Tan, Grain-size-sensitive seismic wave at-
912 tenuation in polycrystalline olivine, *J. Geophys. Res.*, *107*, doi:10.1029/2001JB001225,
913 2002.
- 914 Jaupart, C. & J.-C. Mareschal, Thermal structure and thickness of continental roots,
915 *Lithos*, *48*, 93, 1999.
- 916 Jordan, T. H., The continental tectosphere, *Rev. Geophys. Space Phys.*, *13*, 1, 1975.
- 917 Jordan, T. H., Composition and development of the continental tectosphere, *Nature*, *274*,
918 544, 1978.
- 919 Karato, S.-I., Seismic anisotropy in the deep mantle, boundary layers and the geometry
920 of mantle convection, *Pure Appl. Geophys.*, *151*, 565, 1998.
- 921 Khan, A., Mosegaard, K., Williams, J. G. & Lognonné, P., Does the Moon possess a
922 molten core? Probing the deep lunar interior using results from LLR and Lunar Prospec-
923 tor, *J. Geophys. Res.*, *109*, E09007, doi:10.1029/2004JE002294, 2004.
- 924 Khan, A., J. A. D. Connolly, J. Maclennan, and K. Mosegaard, Joint inversion of seismic
925 and gravity data for lunar composition and thermal state, *Geophys. J. Int.*, *168*, 243,
926 doi:10.1111/j.1365-246X.2006.03200.x, 2007.
- 927 Khan, A., L. Boschi & J. A. D. Connolly, On mantle chemical and thermal heterogeneities
928 and anisotropy as mapped by inversion of global surface wave data, *J. Geophys. Res.*,
929 *114*, B09305, doi:10.1029/2009JB006399, 2009.
- 930 Khan, A., L. Boschi & J. A. D. Connolly, Mapping the Earth's thermo-chemical and
931 anisotropic structure using global surface wave data, *J. Geophys. Res.*, *116*, B01301,
932 doi:10.1029/2010JB007828, 2011.

- 933 Kogan, M.G., and M.K. McNutt, Gravity field over northern Eurasia and variations in
934 the strength of the upper mantle, *Science*, 259, 473, 1993.
- 935 Koren, Z., K. Mosegaard, E. Landa, P. Thore and A. Tarantola, Monte Carlo Estimation
936 and Resolution Analysis of Seismic Background Velocities, *J. Geophys. Res.*, 96, B12,
937 1991.
- 938 Korenaga, J., and S.-I. Karato, A new analysis of experimental data on olivine rheology,
939 *J. Geophys. Res.*, 113, B02403, doi: 10.1029/2007JB005100, 2008.
- 940 Kuskov, O. L., V. A. Kronrod & H. Annersten, Upper mantle temperatures from seismic
941 and geochemical constraints: Implications for the Kaapvaal craton, *Earth Planet. Sci.*
942 *Lett.*, 244, doi:10.1016/j.epsl.2006.02.016, 2006.
- 943 Kuskov, O. L., V. A. Kronrod and A. A. Prokof'ev, Thermal Structure and Thickness of
944 the Lithospheric Mantle Underlying the Siberian Craton from the Kraton and Kimber-
945 lit Superlong Seismic Profiles, *Phys. Solid Earth*, 47, doi:10.1134/S1069351310111011,
946 2011.
- 947 Kustowski, B., G. Ekström & A. M. Dziewonski, Anisotropic shear-wave velocity struc-
948 ture of the Earth's mantle: A global model *J. Geophys. Res.*, 113, B06306, doi:
949 10.1029/2007JB005169, 2008.
- 950 Lebedev, S. & R. D. van der Hilst, Global upper-mantle tomography with the automated
951 multimode inversion of surface and S-wave forms, *Geophys. J. Int.*, 173, 505, 2008.
- 952 Li, A., D. W. Forsyth & K. M. Fischer, Shear velocity structure and azimuthal anisotropy
953 beneath eastern North America from Rayleigh wave inversion, *J. Geophys. Res.*, 108,
954 doi:10.1029/2002JB002259, 2002.

- 955 Long, M. D. & T. W. Becker, Mantle dynamics and seismic anisotropy, *Earth Planet. Sci.*
956 *Lett.*, *297*, 341, 2010.
- 957 Lyubetskaya, T. & J. Korenaga, Chemical composition of Earth's primitive mantle and
958 its variance: 1. Method and results, *J. Geophys. Res.*, *112*, doi:10.1029/2005JB004223,
959 2007.
- 960 McKenzie, D. P., J. A. Jackson & K. F. Priestley, Thermal structure of oceanic and
961 continental lithosphere, *Earth Planet. Sci. Lett.*, *233*, 337, 2005.
- 962 Marone, F, Y. Gung & B. Romanowicz, Three-dimensional radial anisotropic structure of
963 the North American upper mantle from the inversion of surface waveform data, *Geophys.*
964 *J. Int.*, *171*, 206, doi:10.1111/j.1365-246X.2007.03465, 2007.
- 965 Masters, G., G. Laske, H. Bolton & A. M. Dziewonski, The relative behaviour of shear
966 velocity, bulk sound speed, and compressional velocity in the mantle: Implications
967 for chemical and thermal structure, in *Earth's Deep Interior: Mineral Physics and*
968 *Tomography From the Atlantic to the Global Scale*, *Geophys. Monogr. Ser.*, **117**, ed. S.
969 Karato et al., AGU, Washington, D. C, 63, 2000.
- 970 Metropolis, N., Rosenbluth, A. W., Rosenbluth, M. N., Teller, A. H. & Teller, E., Equation
971 of state calculations by fast computing machines, *J. Chem. Phys.*, *21*, 1087, 1953.
- 972 Mitrovica, J.X. and A.M. Forte, A New Inference of Mantle Viscosity Based Upon a Joint
973 Inversion of Convection and Glacial Isostatic Adjustment Data, *Earth Planet. Sci. Lett.*,
974 *225*, 177, 2004.
- 975 Montagner, J. P., Where can seismic anisotropy be detected in the Earth's mantle ? *Pure*
976 *Appl. Geophys.*, *151*, 223, 1998.

- 977 Montagner, J. P. & T. Tanimoto, Global upper mantle tomography of seismic velocities
978 and anisotropies, *J. Geophys. Res.*, *96*, 20337, 1991.
- 979 Montagner, J. P. & B. L. N. Kennett, how to reconcile body-wave and normal-mode
980 reference earth models, *Geophys. J. Int.*, *125*, 229, 1996.
- 981 Mosca, I., *Probabilistic tomography using body-wave, normal-mode and surface-wave data*,
982 Ph.D. Thesis, University of Utrecht, The Netherlands, 2010.
- 983 Mosegaard, K., Resolution analysis of general inverse problems through inverse Monte
984 Carlo sampling, *Inverse Problems*, *14*, 405, 1998.
- 985 Mosegaard, K., Quest for consistency, symmetry and simplicity - The legacy of Albert
986 Tarantola, *Geophysics*, in press, 2011.
- 987 Mosegaard, K. & A. Tarantola, Monte Carlo sampling of solutions to inverse problems,
988 *J. Geophys. Res.*, *100*, 12431, 1995.
- 989 Mosegaard, K. & M. Sambridge, Monte Carlo analysis of inverse problems *Inverse Prob-*
990 *lems*, *18*, R29, 2002.
- 991 Nettles, M. & A. M. Dziewonski, Radially anisotropic shear-velocity structure of the
992 upper mantle globally and beneath North America, *J. Geophys. Res.*, *113*, B02303,
993 doi:10.1029/2006JB004819, 2008.
- 994 Panning, M. & B. Romanowicz, A three-dimensional radially anisotropic model of shear
995 velocity in the whole mantle, *Geophys. J. Int.*, *167*, 361, 2006.
- 996 Priestley, K. F. & D. P. McKenzie, The thermal structure of the lithosphere from shear
997 wave velocities, *Earth Planet. Sci. Lett.*, *244*, 285, 2006.
- 998 Rawlinson, N., S. Pozgay & S. Fishwick, Seismic tomography: A window into deep Earth,
999 *Phys. Earth Planet. Int.*, *178*, 101, 2010.

- 1000 Ricard, Y., L. Fleitout, and C. Froideveaux, Geoid heights and lithospheric stresses for a
1001 dynamic Earth, *Ann. Geophys.*, *2*, 267, 1984.
- 1002 Ricard, Y., M. Richards, C. Lithgow-Bertelloni, and Y. Le Stunff, A geodynamic model
1003 of mantle density heterogeneity, *J. Geophys. Res.*, *98*, 21895, 1993.
- 1004 Ritsema, J, H. J. Van Heijst & J. H. Woodhouse, Complex shear wave velocity structure
1005 imaged beneath Africa and Iceland, *Science*, *286*, 1925, 1999.
- 1006 Ritsema, J, H. J. Van Heijst & J. H. Woodhouse, Global transition zone tomography, *J.*
1007 *Geophys. Res.*, *109*, B02302, doi:10.1029/2003JB002610, 2004.
- 1008 Ritsema, J, W. Xu, L. Stixrude & C. Lithgow-Bertelloni, Estimates of the transition
1009 zone temperature in a mechanically mixed upper mantle, *Earth Planet. Sci. Lett.*, *244*,
1010 doi:10.1016/j.epsl.2008.10.024, 2009.
- 1011 Ritsema, J., H. J. van Heijst, A. Deuss, and J. H. Woodhouse, S40RTS: a degree-40
1012 shear velocity model for the mantle from new Rayleigh wave dispersion, teleseismic
1013 traveltimes, and normal-mode splitting function measurements, *Geophys. J. Int.*, *184*,
1014 doi:10.1111/j.1365-246X.2010.04884.x, 2011.
- 1015 Ritzwoller, M. H., N. M. Shapiro & S.-J. Zhong, Cooling history of the Pacific lithosphere,
1016 *Earth Planet. Sci. Lett.*, *226*, 69, 2004.
- 1017 Romanowicz, B., Global mantle tomography: Progress status in the past 10 years, *Ann.*
1018 *Rev. Earth Planet. Sci.*, *31*, 303, 2003.
- 1019 Rudnick, R. L., W. F. McDonough & R. J. O'Connell, Thermal structure, thickness and
1020 composition of continental lithosphere, *Chem. Geol.*, *145*, 395, 1998.
- 1021 Röhm, A. H. E., R. Snieder, S. Goes & J. Trampert, Thermal structure of continental
1022 upper mantle inferred from S-wave velocity and surface heat flow, *Earth Planet. Sci.*

- 1023 *Lett.*, 181, 395, 2000.
- 1024 Sambridge, M. & K. Mosegaard, Monte Carlo methods in Geophysical inverse problems,
1025 *Rev. Geophys.*, 40, doi:10.1029/2000RG000089, 2002.
- 1026 Sengupta, M. K. & M. N. Toksöz, Three-dimensional model of seismic velocity variation
1027 in the Earth's mantle, *Geophys. Res. Lett.*, 3, 84, 1977.
- 1028 Shapiro, N. M. & M. H. Ritzwoller, Monte-Carlo inversion for a global shear-velocity
1029 model of the crust and upper mantle, *Geophys. J. Int.*, 151, 88, 2002.
- 1030 Shapiro, N. M. & M. H. Ritzwoller, Thermodynamic constraints on seismic inversions,
1031 *Geophys. J. Int.*, 157, doi: 10.1111/j.1365-246X.2004.02254.x, 2004.
- 1032 Sigloch, K., N. McQuarrie & G. Nolet, Two-stage subduction history under North America
1033 inferred from multiple-frequency tomography, *Nature Geoscience*, doi:10.1038/ngeo231,
1034 2008.
- 1035 Simmons, N. A., A. M. Forte & S. P. Grand, Joint seismic, geodynamic and mineral
1036 physical constraints on three-dimensional mantle heterogeneity: Implications for the
1037 relative importance of thermal versus compositional heterogeneity *Geophys. J. Int.*,
1038 177, 1284, 2009,
- 1039 Smith, W. H. F. & P. Wessel, Gridding with continuous curvature splines in tension,
1040 *Geophysics*, 55, 293, 1990.
- 1041 Sobolev, S. V. et al., Upper mantle temperatures from teleseismic tomography of French
1042 Massif Central including effects of composition, mineral reactions, anharmonicity,
1043 anelasticity and partial melt, *Earth Planet. Sci. Lett.*, 157, 193, 1996.
- 1044 Soldati, G., L. Boschi, F. Deschamps, and D. Giardini, Inferring radial models of man-
1045 tle viscosity from gravity (GRACE) data and an evolutionary algorithm, *Phys. Earth*

- 1046 *Planet. Inter.*, 176, 19, 2009.
- 1047 Stixrude, L., and C. Lithgow-Bertelloni, Mineralogy and elasticity of the oceanic
1048 upper mantle: Origin of the low-velocity zone, *J. Geophys. Res.*, 110, B03204,
1049 doi:10.1029/2004JB002965, 2005.
- 1050 Tanimoto, T. & D. L. Anderson, Mapping convection in the mantle, *Geophys. Res. Lett.*,
1051 11, 287, 1984.
- 1052 Tapley, B., J. Ries, S. Bettadpur, D. Chambers, M. Cheng, F. Condi, B. Gunter, Z. Kang,
1053 P. Nagel, R. Pastor, T. Pekker, S. poole, and F. Wang, GGM02 - An improved Earth
1054 gravity field model from GRACE, *J. Geodesy*, 79, 467, 2005.
- 1055 Tarantola, A., *Inverse problem theory and methods for model parameter estimation*, SIAM,
1056 Philadelphia, USA, 2005.
- 1057 Tarantola, A., and B. Valette, Inverse problems: Quest for information, *J. Geophys.*, 50,
1058 159, 1982.
- 1059 Tian, Y., K. Sigloch & G. Nolet, Multiple-frequency SH-wave tomography of the
1060 western US upper mantle, *Geophys. J. Int.*, 178(3), 1384-1402, doi:10.1111/j.1365-
1061 246X.2009.04225.x, 2009.
- 1062 Trampert, J., Global seismic tomography: the inverse problem and beyond, *Inverse Prob-*
1063 *lems*, 14, 371, doi: 10.1088/0266-5611/14/3/002, 1998.
- 1064 Trampert, J. & J. H. Woodhouse, Assessment of global phase velocities, *Geophys. J. Int.*,
1065 144, 165, 2001.
- 1066 Trampert, J. & J. H. Van Heijst, Global Azimuthal Anisotropy in the Transition Zone,
1067 *Science*, 296, 1297, doi:10.1126/science.1070264, 2002.

- 1068 Trampert, J., Deschamps, F., Resovsky, J. & D. Yuen, 2004. Chemical heterogeneities
1069 throughout the lower mantle, *Science*, *306*, 853, 2004.
- 1070 Trampert, J. & R. D. van der Hilst, Towards a quantitative interpretation of global seismic
1071 tomography, in *Earth's Deep Mantle: Structure, Composition and Evolution*, Geophys.
1072 Monogr. Ser., vol. 160, eds. R. D. van der Hilst et al., AGU, Washington, D. C., 47,
1073 2005.
- 1074 Van der Lee, S. & G. Nolet, Seismic image of the subducted trailing fragments of the
1075 Farallon plate, *Nature*, *386*, 266, 1997a.
- 1076 Van der Lee, S. & G. Nolet, Upper-mantle *S*-velocity structure of North America, *J.*
1077 *Geophys. Res.*, *102*, 22815, 1997b.
- 1078 Van der Lee, S. & A. Frederiksen, Surface wave tomography applied to the North American
1079 upper mantle, *Seismic Earth: Array Analysis of Broadband Seismograms*, Geophys.
1080 Monogr. Ser., vol. 157, eds. A. Levander and G. Nolet, AGU, Washington, D. C., 67,
1081 2005.
- 1082 van Gerven, L., F. Deschamps, and R.D. van der Hilst, Geophysical evidence for chem-
1083 ical variations in the Australian continental mantle, *Geophys. Res. Lett.*, *31*, L17607,
1084 doi:10.1029/2004GL020307, 2004.
- 1085 Visser, K., Trampert, J. & B. L. N. Kennett, Global anisotropic phase-velocity maps for
1086 higher mode Love and Rayleigh waves, *Geophys. J. Int.*, *172*, 1016, 2008a.
- 1087 Visser, K., Trampert, J., S. Lebedev & B. L. N. Kennett, Probability of radial anisotropy
1088 in the deep mantle, *Earth Planet. Sci. Lett.*, doi:10.1016/j.epsl.2008.03.041, 2008b.
- 1089 Wessel, P. & W. H. F. Smith, New, improved version of Generic Mapping Tools released,
1090 *EOS trans. AGU*, *79*, 579, 1998.

- 1091 Wookey, J., J.-M. Kendall & G. Barruol, Mid-mantle deformation inferred from seismic
1092 anisotropy. *Nature*, *415*, 777, 2002.
- 1093 Xu, W., C. Lithgow-Bertelloni, L. Stixrude & J. Ritsema, The effect of bulk com-
1094 position and temperature on mantle seismic structure, *Earth Planet. Sci. Lett.*,
1095 doi:10.1016/j.epsl.2008.08.012, 2008.
- 1096 Yoshida, M., and T. Nakakuki, Effects on the long-wavelength geoid anomaly of lateral
1097 viscosity variations caused by stiff subducting slabs, weak plate margins and lower
1098 mantle rheology, *Phys. Earth Planet. Inter.*, *172*, 278, 2009.
- 1099 Yuan, H. & B. Romanowicz, Lithospheric layering in the North American craton, *Nature*,
1100 *466*, doi:10.1038/nature09332, 2010.
- 1101 Yuan, H., B. Romanowicz, K. Fisher & D. Abt, 3-D shear wave radially and azimuthally
1102 anisotropic velocity model of the North American upper mantle, *Geophys. J. Int.*, *184*,
1103 doi: 10.1111/j.1365-246X.2010.04901.x, 2010.

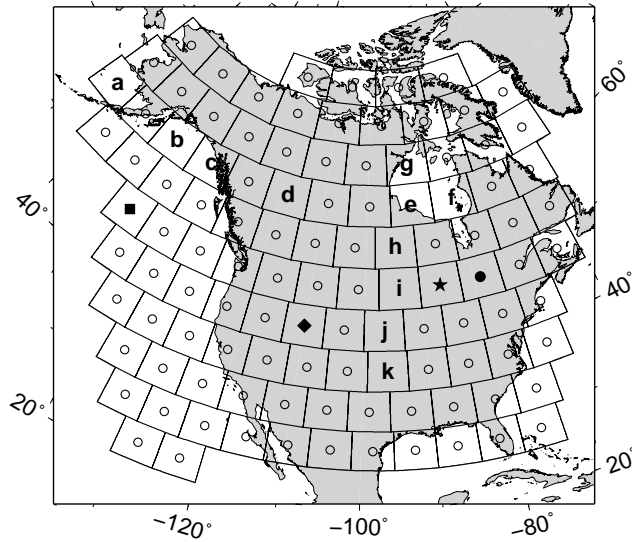


Figure 1. Parameterization of the model. Dots at the center of each pixel denote the locations at which properties are defined laterally. Grid spacing is 5° . Radially the model is parameterized in terms of layers (see section 4.1 for further discussion). Symbols (diamond, circle, square and star) indicate the location for which 1D marginal *pdfs* are shown in figures 3-6. Letters a-f refer to the locations for which radial shear-wave velocity profiles are displayed in figure 9, while letters e,g-k refer to figure 10.

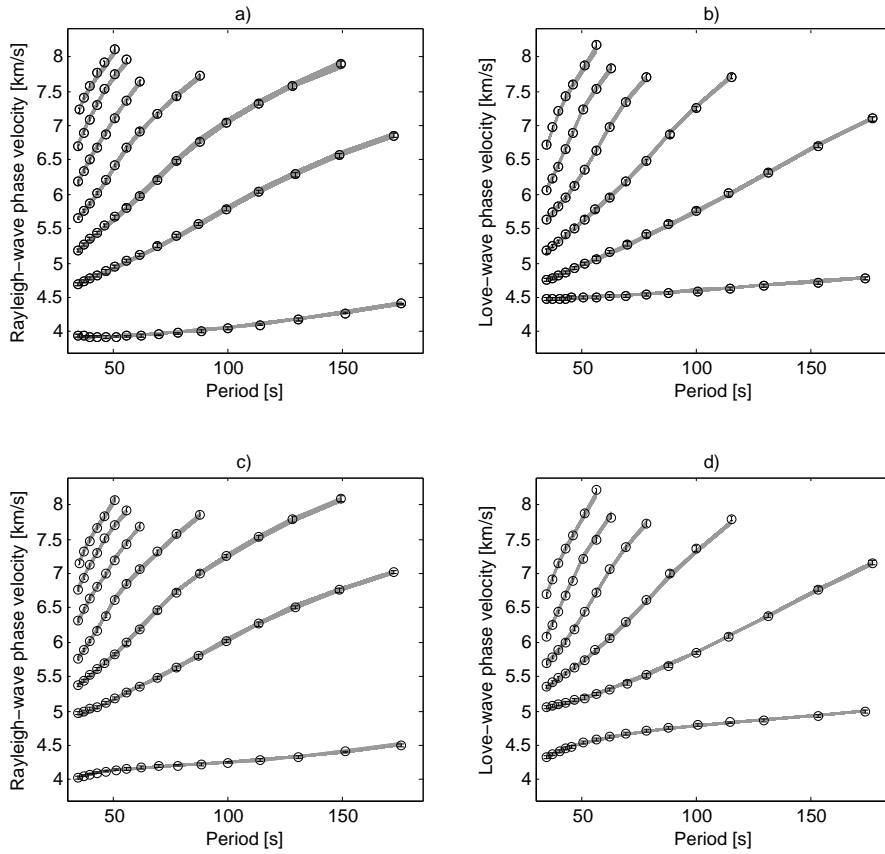


Figure 2. Datafit. Comparison of calculated (gray lines) and observed Rayleigh and Love-wave phase-velocities (circles), including uncertainties (error bars) at two different locations, which are shown in figure 1 (a,b - filled square and c,d - filled circle).

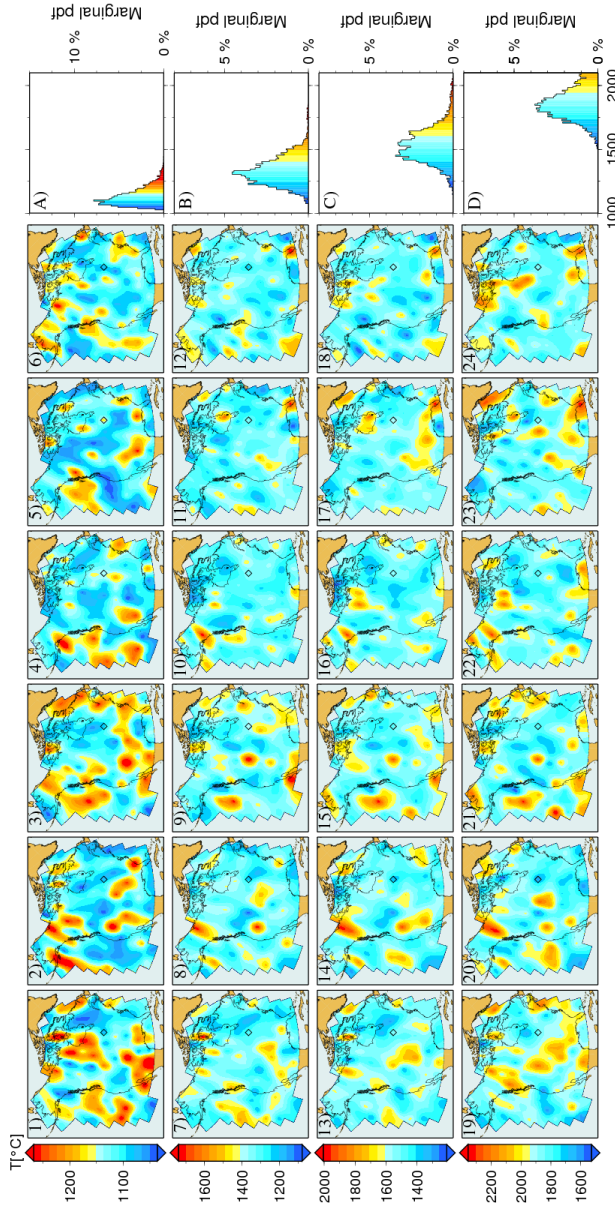


Figure 3. Prior thermal movie. The first six maps of each panel show six thermal models that are picked randomly from the prior distribution at a particular depth: first panel (plots labeled 1-6, A) - 100 km, second panel (plots labeled 7-12, B) - 300 km, third panel (plots labeled 13-18, C) - 500 km and fourth panel (plots labeled 19-24, D) - 1000 km. Plots labeled A-D indicate the prior marginal mantle temperature distribution at these depths for the pixel identified by the diamond (see also figure 1). For all maps shown here and in the following, data were gridded using continuous curvature splines (Smith & Wessel, 1990) in tension method (with tension set to 0.15) as implemented in

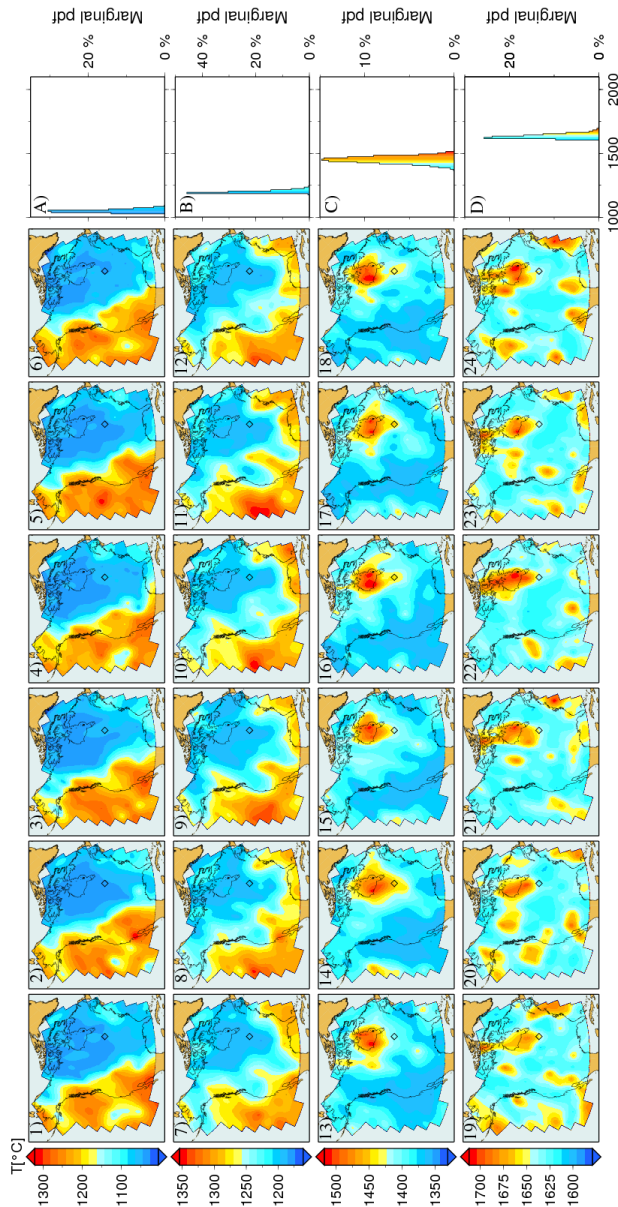


Figure 4. Posterior thermal movie. The first six maps of each panel show six thermal models that are picked randomly from the posterior distribution at the same depths as in figure 2, i.e. 100 km (1-6), 300 km (7-12), 500 km (13-18) and 1000 km (19-24) depth. Plots labeled A-D indicate the posterior marginal mantle temperature distribution at these depths for the pixel identified by the diamond (see also figure 1). Note that prior and posterior colourbars do not overlap in temperature range for a given depth, but that the temperature axis for the 1D marginal prior and posterior distributions have the same range.

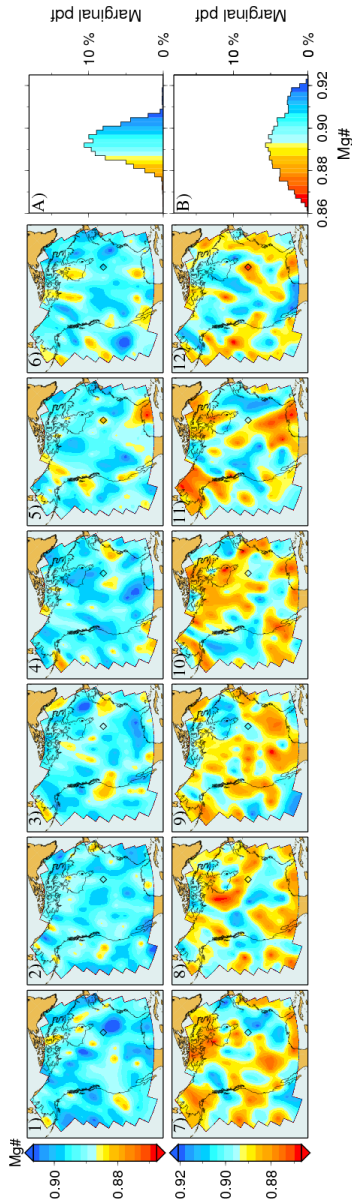


Figure 5. Prior compositional movie. The first six maps of each panel show six compositional (in terms of Mg#) models that are picked randomly from the prior distribution at depths of 100 km (1-6) and 1000 km (7-12). Plots labeled A and B indicate prior marginal distribution of upper and lower mantle composition (Mg#), respectively, at the above depths at the location of the pixel identified by the diamond (see also figure 1).

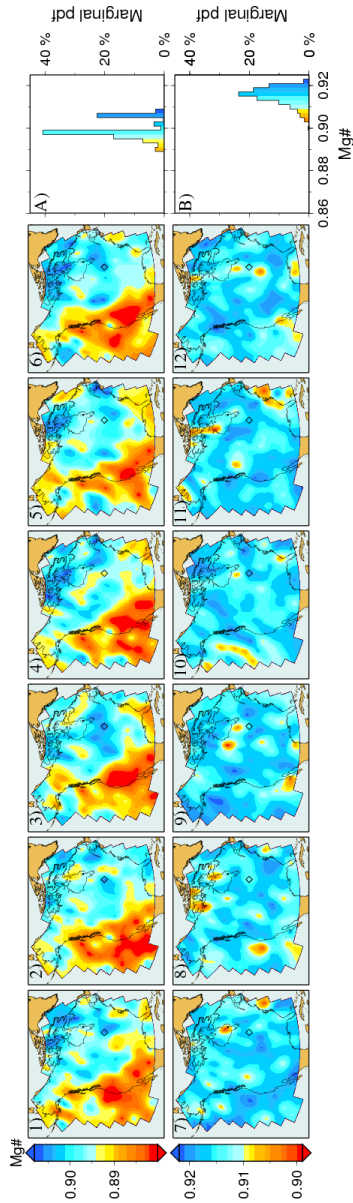


Figure 6. Posterior compositional movie. The first six maps of each panel show six compositional (in terms of Mg#) models that are picked randomly from the posterior distribution at depths of 100 km (1-6) and 1000 km (7-12). Plots labeled A and B indicate posterior marginal distribution of upper and lower mantle composition (Mg#), respectively, at the above depths at the location of the pixel identified by the diamond (see also figure 1). Note that prior and posterior colourbars do not overlap in Mg# range for a given depth, but that the Mg#-axis for the 1D marginal prior and posterior distributions have the same range.

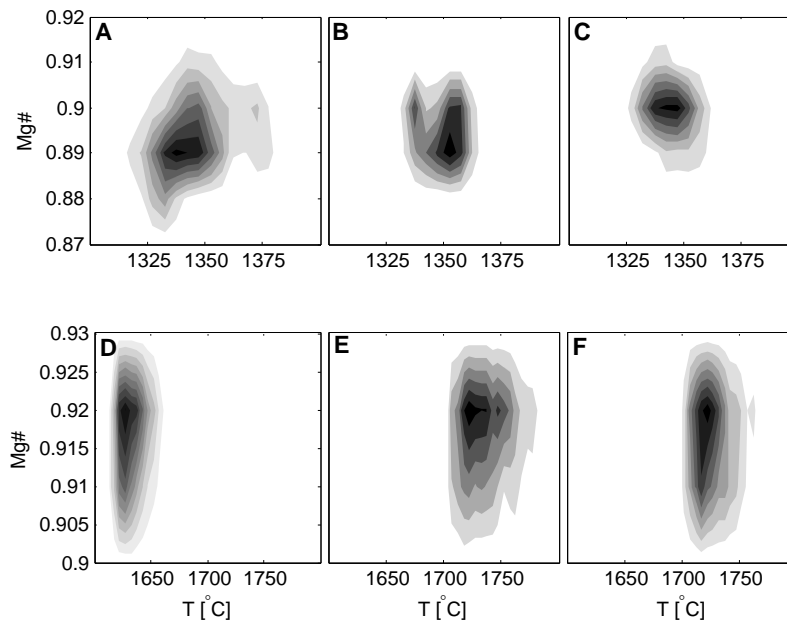


Figure 7. Two-dimensional (2D) marginal posterior probability density functions showing correlation between temperature and composition (here Mg#) for three different tectonic settings in the upper and lower continental lithosphere (A,D), young continental lithosphere (B,E) and old continental lithosphere (C,F). Location of pixels are indicated in figure 1 by a filled square (A,D), a filled diamond (B,E) and a filled circle (C,F). The 2D marginals are envisioned as contours directly relating their probability of

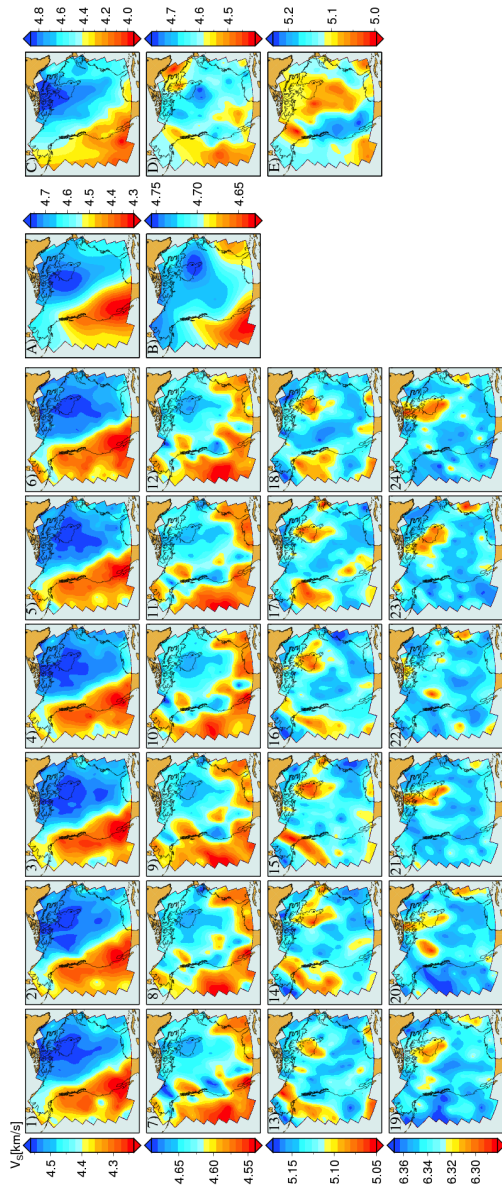


Figure 8. Posterior isotropic shear-wave velocity movie. In each panel the six maps represent six shear-wave velocity models that are picked randomly from the posterior distribution at depths of 100 km (1-6), 300 km (7-12), 500 km (13-18) and 1000 km (19-24), respectively. Note that prior and posterior colourbars do not bracket similar V_S ranges at individual depths. For comparison other regional shear-wave velocity models have been included. Plots A (at 100 km depth) and B (at 300 km depth) show the model of *Nettles & Dziewonski* [2008]; plots E (100 km), F (300 km) and G (500 km) depict the model of *Yuan et al.* [2010]. Note differences in absolute shear-wave velocities (colourbars)



Figure 9. Selected shear-wave velocity models beneath different tectonic settings in the

upper mantle and transition zone (A) and lower transition zone and mantle (B) : Oceanic

D R A F T

March 28, 2011, 11:10am

D R A F T

(a-c), young continent (d) and old stable continent (e,f). Profiles encompass all sampled

models. Geographic location of letters are indicated in figure 1.

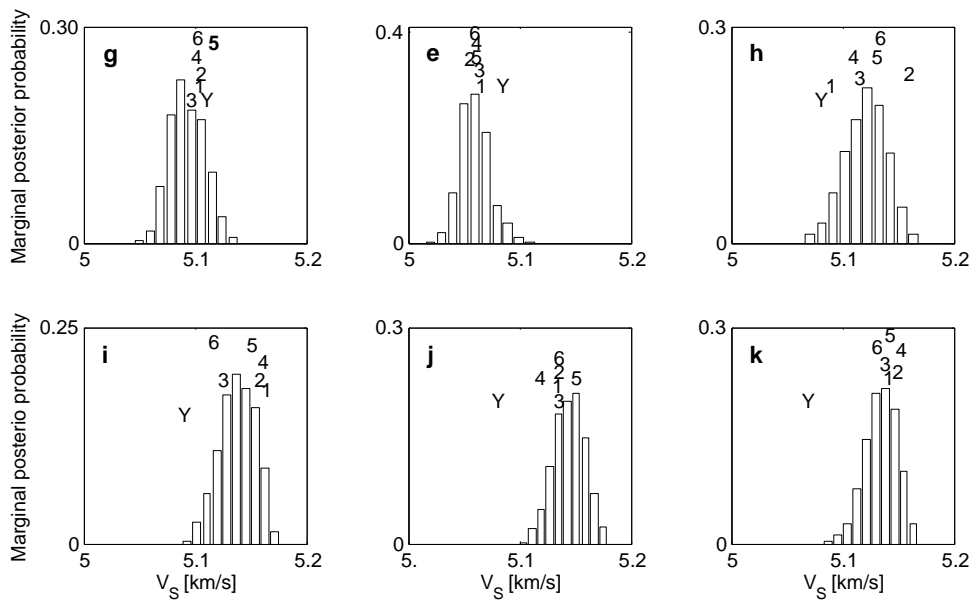


Figure 10. Marginal posterior probability distributions of sampled isotropic shear-wave velocities at 500 km depth beneath the North American continent. Location of pixels are shown in figure 1, with letters identifying the specific pixel. Numbers 1-6 above the distributions indicate the S -wave velocity for each of the six posterior models shown in figure 9 at 500 km depth (plots 13-18), while 'Y' is the shear-wave velocity at the same depth for the model of *Yuan et al.* [2010].

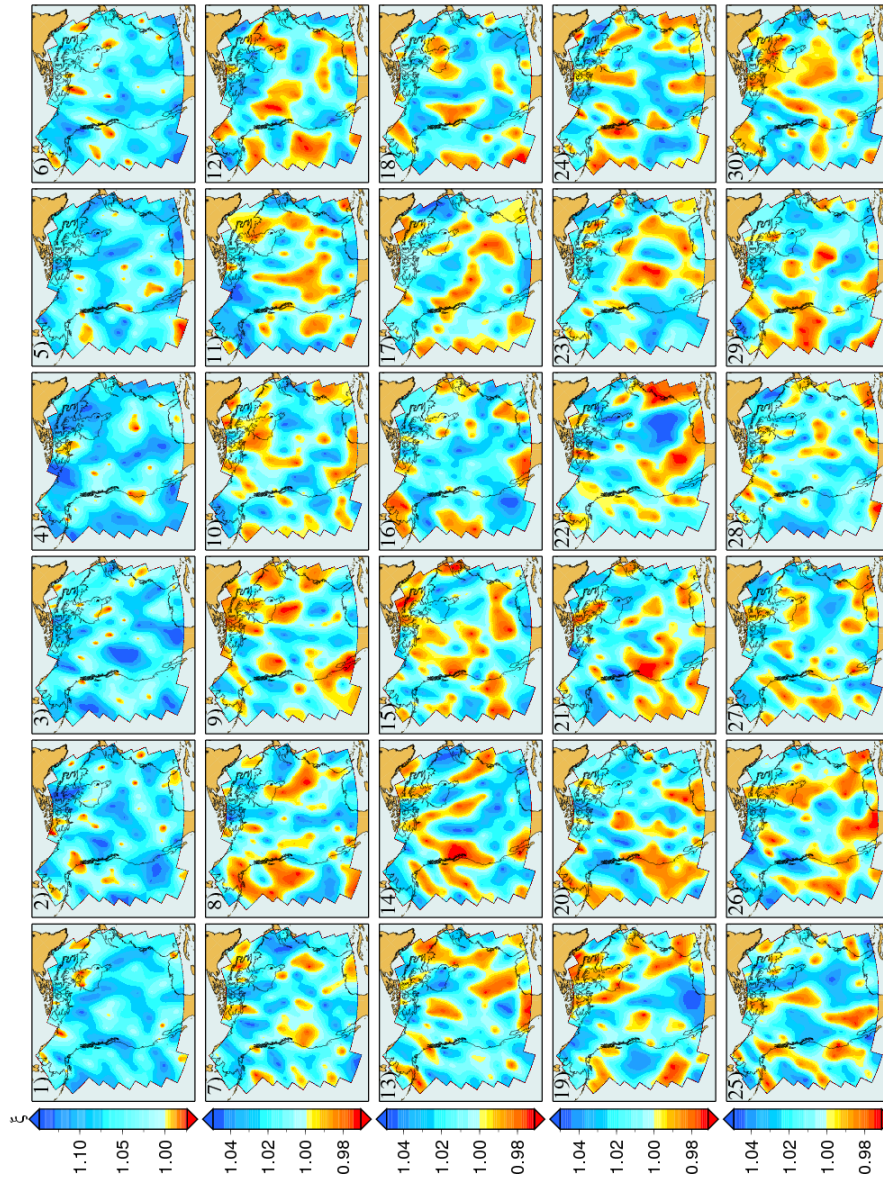


Figure 11. Prior shear-wave anisotropy movie. In each panel the six maps represent six different shear-wave anisotropy models that are picked randomly from the prior distribution at depths of 100 km (1-6), 300 km (7-12), 500 km (13-18) and 1000 km (19-24), respectively.

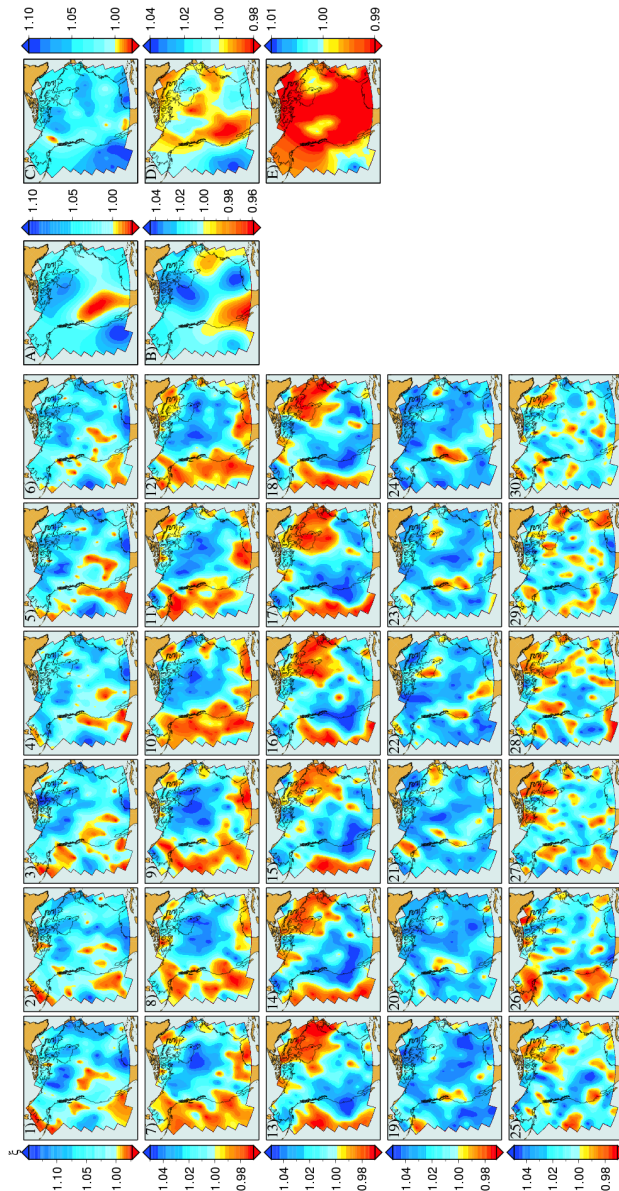


Figure 12. Posterior shear-wave anisotropy movie. In each panel the six maps represent six different shear-wave anisotropy models that are picked randomly from the posterior distribution at depths of 100 km (1-6), 300 km (7-12), 500 km (13-18), 1000 km (19-24) and 1800 km (25-30), respectively. Note that prior and posterior colourbars do not bracket similar ξ ranges. For comparison other regional anisotropic tomography models have been included. Plots A (at 100 km depth) and B (at 300 km depth) show the model of *Nettles & Dziewonski* [2008]; plots E (100 km), F (300 km) and G (500 km) depict the model of *Yuan et al.* [2010]. Note differences in colourbars, i.e. absolute shear-wave anisotropy,

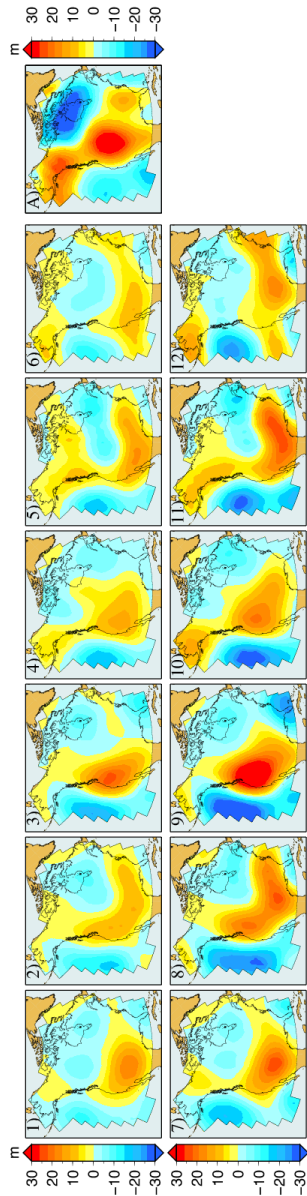
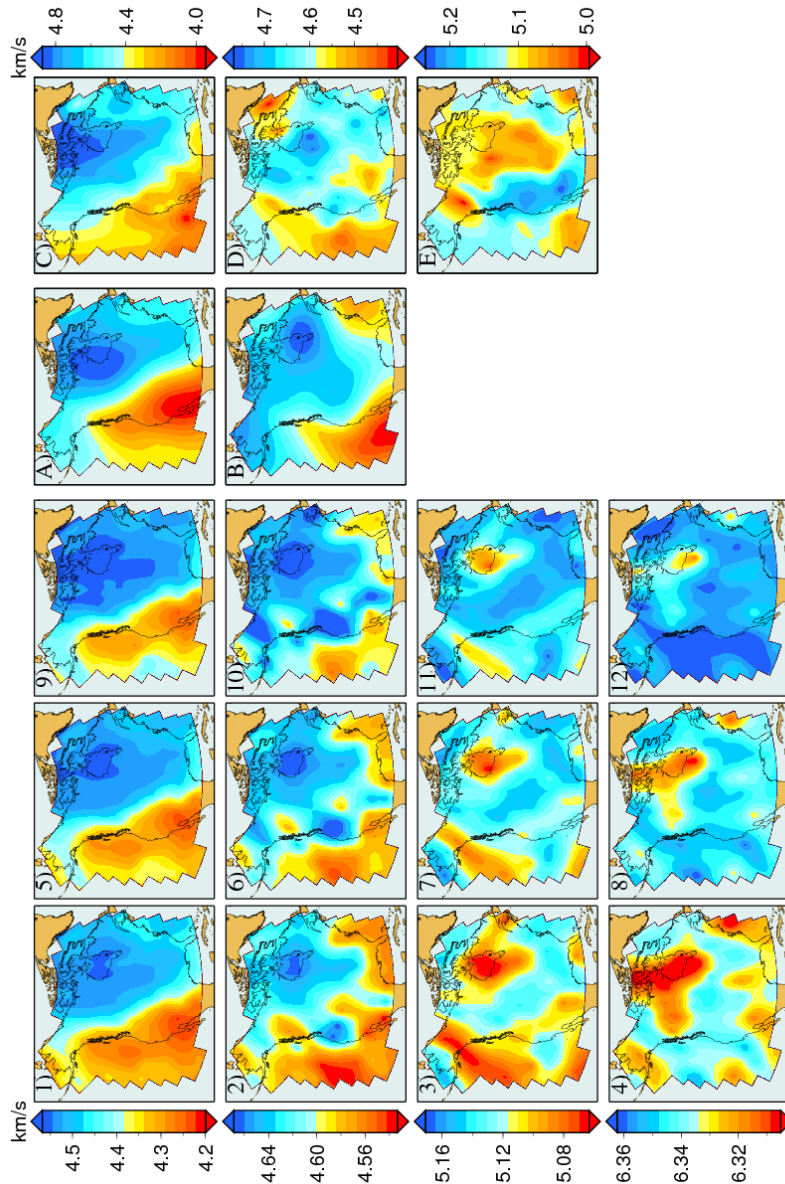
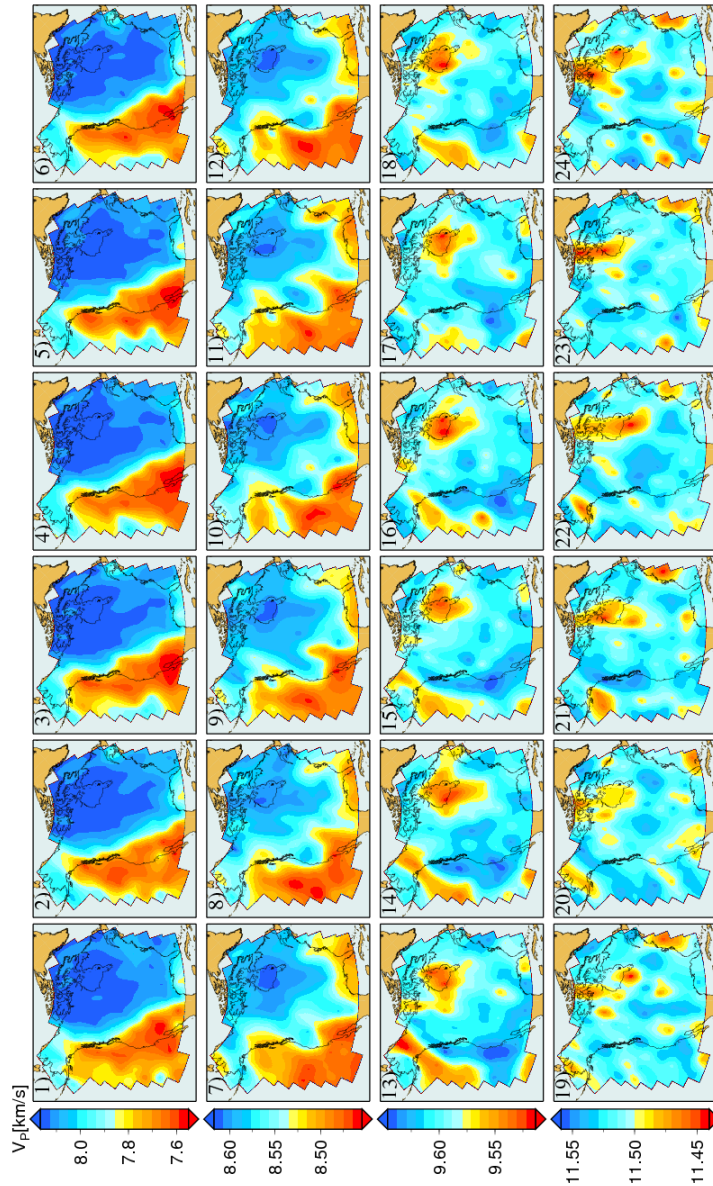


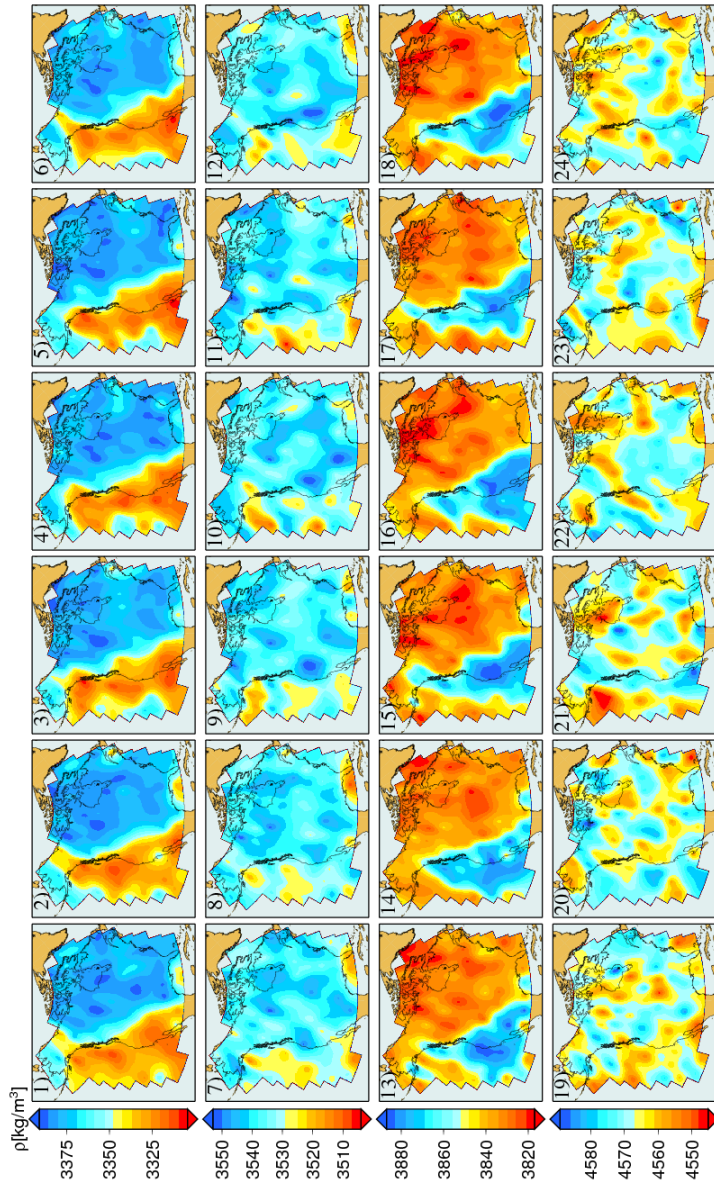
Figure 13. Reconstructed geoid anomalies for the six posterior density models shown in figure S3 (online supporting material) using a continental average viscosity profile (plots 1-6) and regionally averaged viscosity profiles (plots 7-12). Viscosity profiles are shown in online supporting material (figure S4). Only harmonic degrees 6 to 20 are used. For further details see main text. For comparison, plot A shows the observed geoid GGM02 of *Tapley et al.* [2005] for the same harmonic degrees.



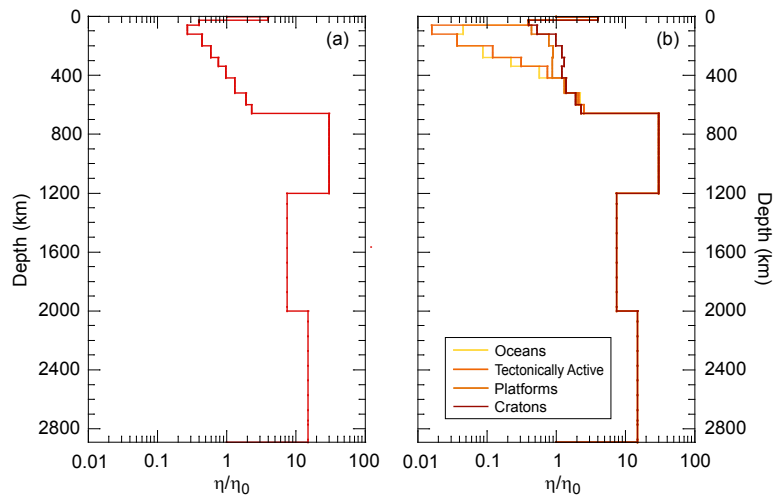
Online supporting material - Figure S1. Mean isotropic shear-wave velocities (plots 5-8) and mean \pm standard deviation (plots 1-4 and 9-12) computed directly from the posterior probability distributions. Panel 1 is at a depth of 100 km, panel 2 at 300 km depth, panel 3 at 500 km depth and panel 4 at a depth of 1000 km, respectively. For comparison other regional shear-wave velocity models have been included. Plots A (at 100 km depth) and B (at 300 km depth) show the model of *Nettles & Dziewonski* [2008]; plots E (100 km), F (300 km) and G (500 km) depict the model of *Yuan et al.* [2010]. Note differences in absolute shear-wave velocities (colourbars) between present and previous models.



Online supporting material - Figure S2. Posterior isotropic P -wave velocity movie. In each panel the six maps represent six P -wave velocity models that are picked randomly from the posterior distribution at depths of 100 km (1-6), 300 km (7-12), 500 km (13-18) and 1000 km (19-24), respectively.



Online supporting material - Figure S3. Posterior density model movie. In each panel the six maps represent six density models that are picked randomly from the posterior distribution at depths of 100 km (1-6), 300 km (7-12), 500 km (13-18) and 1000 km (19-24), respectively.



On-

line supporting material - Figure S4. The two viscosity models considered in this study.

In (a), the upper mantle viscosity is averaged over the entire study region (continental

average), whereas in (b) the models represent averages within four tectonically coherent

D R A F T

March 28, 2011, 11:10am

D R A F T

regions (regional average, see legend).